



HAL
open science

Evolution of microstructure after irradiation creep in several austenitic steels irradiated up to 120 dpa at 320°C

Alexandra Renault-Laborne, J. Garnier, J. Malaplate, P. Gavaille, F. Sefta, B. Tanguy

► To cite this version:

Alexandra Renault-Laborne, J. Garnier, J. Malaplate, P. Gavaille, F. Sefta, et al.. Evolution of microstructure after irradiation creep in several austenitic steels irradiated up to 120 dpa at 320°C. Journal of Nuclear Materials, 2016, 475, pp.209-226. 10.1016/j.jnucmat.2016.04.020 . cea-02381473

HAL Id: cea-02381473

<https://cea.hal.science/cea-02381473>

Submitted on 23 Jan 2020

HAL is a multi-disciplinary open access archive for the deposit and dissemination of scientific research documents, whether they are published or not. The documents may come from teaching and research institutions in France or abroad, or from public or private research centers.

L'archive ouverte pluridisciplinaire **HAL**, est destinée au dépôt et à la diffusion de documents scientifiques de niveau recherche, publiés ou non, émanant des établissements d'enseignement et de recherche français ou étrangers, des laboratoires publics ou privés.



Distributed under a Creative Commons Attribution 4.0 International License

Evolution of microstructure after irradiation creep in several austenitic steels irradiated up to 120 dpa at 320 °C

A. Renault-Laborne ^{a,*}, J. Garnier ^a, J. Malaplate ^a, P. Gavaille ^b, F. Sefta ^c, B. Tanguy ^b

^a DEN-Service de Recherches Métallurgiques Appliquées, CEA, Université Paris-Saclay, F-91191, Gif-sur-Yvette, France

^b DEN-Service d'Etudes des Matériaux Irradiés, CEA, Université Paris-Saclay, F-91191, Gif-sur-Yvette, France

^c EDF R&D, MMC, Site des Renardières, F-77818, Morêt-sur-Loing Cedex, France

Irradiation creep was investigated in different austenitic steels. Pressurized tubes with stresses of 127–220 MPa were irradiated in BOR-60 at 320 °C to 120 dpa. Creep behavior was dependent on both chemical composition and metallurgical state of steels.

Different steels irradiated with and without stress were examined by TEM. Without stress, the irradiation produced high densities of dislocation lines and Frank loops and, depending on the type of steels, precipitates. Stress induced an increase of the precipitate mean size and density and, for some grades, an increase of the mean loop size and a decrease of their density. An anisotropy of Frank loop density or size induced by stress was not observed systematically. Dislocation line microstructure seems not to be different between the stressed and unstressed specimens. No cavities were detectable in these specimens.

By comparing with the data from this work, the main irradiation creep models are discussed.

1. Introduction

The study of irradiation creep is of interest to assess the performance of austenitic stainless steels for the internal structures of pressurized water reactors (PWRs). Many irradiation creep data were experimentally obtained after neutron or ion irradiation.

Most of the macroscopic creep properties of austenitic stainless steels have been obtained at high irradiation temperatures (≥ 390 °C), where swelling can be notable, and under fast neutron-irradiations [1–8]. In these conditions, limited data on the effects of stress on the microstructure during irradiation have been reported [1,8–14].

Few studies on irradiation creep properties have been reported on neutron irradiated steel for lower irradiation temperatures, i.e. 290–390 °C. They were mainly devoted to the determination of macroscopic properties.

Grossbeck et al., Foster et al. and Garnier et al. [15–19] have reported irradiation creep data measured in mixed neutron spectrum reactors and fast neutron spectrum reactors. They have shown

that the steady-state irradiation creep rate is higher in mixed reactors than in fast reactors (Oak Ridge Research (ORR)/Halden/Osiris reactors vs. Fast Flux Test Facility (FFTF)/BOR-60 fast reactors). The values of steady-state irradiation creep compliance of SA 304L and CW 316 obtained by Foster et al. [16,17] after irradiation in the HALDEN reactor was found to be the same order of magnitude as those by Garnier et al. in the OSIRIS reactor [18,19]. The higher creep rates are believed to result from either the lower flux in the Osiris experiment or from its higher level of thermal neutrons. Garnier et al. [18,19] have also highlighted that the threshold stress \times dose for irradiation creep is much lower in mixed reactor than in fast reactor (respectively, ~ 200 and ~ 1000 MPa dpa). In these studies, the specimens are pressurized tubes of solution-annealed 304L (SA 304L) and cold-worked 316 (CW 316) austenitic stainless steels and of cold-worked prime candidate alloy (CW PCA). This latter alloy is a Ti-modified 14Cr–16Ni austenitic stainless steel. SA 304 has a higher steady-state irradiation creep rate than CW 316. The value of creep rate of CW PCA was found to be intermediate between those obtained in the other two steels.

Microstructural studies have often been conducted on specimens which were neutron-, ion- or electron-irradiated up to a very low dose under stress [20–28]. They were sometimes based on

* Corresponding author.

E-mail address: alexandra.renault@cea.fr (A. Renault-Laborne).

nickel rich specimens.

Most of the microstructural studies are exclusively based on the Frank loop distributions in terms of number density and mean size within the same grain. Nevertheless, at low dose, the density and size of Frank loops has not reached a saturation value (typically, below 3–5 dpa at a temperature of at least 320 °C [29,30]). Studies of Frank loop anisotropy often gave contradictory response [31,32]. Sometimes, populations were enhanced in proportion to the normal stress on the loop plane, sometimes not.

Moreover, these loops constitute only a part of the important features of irradiated austenitic steels. Indeed, recent quantitative studies using several combined techniques of transmission electron microscopy (TEM) and atom probe tomography (APT) [33–45] have shown the presence of precipitates in the austenitic stainless steels after neutron-irradiation. Their number density and size were sometimes found to be of the same order of magnitude as those of Frank loops. So, the possible role of precipitates in irradiation creep should not be ignored.

Microstructural studies are a tool of interest for the discrimination of the following principal models of irradiation creep: stress-induced preferred nucleation (SIPN) of interstitial loops, stress induced preferred absorption of points defects by dislocations favorably oriented to an applied stress (SIPA) and stress induced climb and glide (SICG) [8,11,20,21,23–26,46–49]. Indeed, they allow one to study the possible effect of stress on the partitioning of Frank loops between the four sets of {111} planes of the austenitic (γ) matrix in terms of density and size.

Nowadays, the effect of chemical composition and metallurgical state on irradiation creep behavior under PWR relevant temperature up to high doses is still lacking.

The purpose of this work is to clarify the relationship between microstructure and creep behavior through TEM observations on the different types of austenitic steel irradiated in the BOR-60 fast reactor, at 320 °C and with and without applied stresses. By means of the chemical and metallurgical variations, the effect of stress on microstructural evolution was carefully examined.

2. Experimental details

2.1. Materials

Different steel grades were investigated. Two grades are representative of the materials for the core internals of French PWRs, i.e. SA 304L and CW 316. Nine other materials with chemical and metallurgical variations have been chosen for this work. These materials are SA 316, CW titanium-stabilized 316 (CW 316Ti), SA titanium-stabilized 316 (SA 316Ti), CW high purity 316 (CW HP316), CW high purity silicon-modified 316 (CW HP316Si), SA 321, SA NMF18, CW N9 and SA N9.

Among the different grades reported here, 304 is considered as a base. The higher molybdenum and nickel content in the 316 grade allows it to increase corrosion resistance. In the 316Ti grade, an amount of titanium of about 0.3% in weight is added to retard the dislocation mobility. It was proven to exhibit a good resistance to high dose neutron irradiation, especially above 400 °C, in the frame of the programs related to fuel assemblies for fast breeder reactors. 321 is a titanium-stabilized austenitic stainless steel. It was developed as an alloy in which the detrimental effects of carbon were suppressed by addition of a higher amount of titanium, compared to 316Ti. It is the only grade which is not an as-received material. For the two high purity 316 grades (HP316 and HP316Si), the elaboration of materials was carried out controlling the minor elements (low phosphorus, sulphur, etc ...). The first material has a low silicon and carbon content (HP316) and the second material has a silicon and carbon content typical of the current materials

(HP316Si). In 304L, the carbon content is reduced to prevent carbide precipitation. In the NMF18 grade, manganese and nitrogen, two austenite stabilizers, partially replace nickel. Manganese was chosen due to its lower price than nickel. This latter grade also contains a relatively high amount of carbon. N9 is a 25% nickel, 12% chromium austenitic alloy stabilized with titanium (about 0.51% in weight). Strong addition of nickel is known to lower work hardening and the opposite effect is observed with decreasing of the chromium content.

Their metallurgical state, cold-working level, chemical composition and grain size are listed in Table 1.

2.2. Irradiation conditions for gas-pressurized tubes and tensile specimens, and irradiation creep tests

The experiment in the BOR-60 sodium-cooled fast neutron reactor was conducted in Row 5. The specimens were contained in seven perforated cylindrical baskets. These seven baskets were placed in a rig and irradiated in direct contact with the flowing sodium. Dosimeters and thermocouples were respectively placed at the level of each basket and at the coolant inlet and outlet of the rig. The lowest and highest temperatures were respectively ~315 °C and ~325 °C. The increase of temperature of sodium in the rig varied from 8.6 to 11.5 °C (averaged over a cycle). The temperature of all the specimens remained close to ~320 °C.

Pressurized tubes were placed side-by-side in BOR-60 to provide identical irradiations within the same basket. This basket was located on level #1 and was not necessarily kept in the same dose rate from one irradiation cycle to the next, which occasionally resulted in small dose differences from one irradiation cycle to the next. Around 22 dpa are produced for the five annual irradiation cycles and 8.4 dpa for the preliminary sixth months cycle. The dose rate ranged from $\sim 9 \cdot 10^{-7}$ to $\sim 1 \cdot 10^{-6}$ dpa/s.

Thin-walled inert gas-filled tubes with welded end-caps were fabricated from different steel grades. The shape of the creep tubes is given in Fig. 1. The tubes were 55 mm in length and 5.65 mm in inner diameter. Their length between the two grooves was 36 mm. The tube wall was 0.45 mm thick. Pressurization was accomplished with argon gas, except for the CW 316Ti tube pressurized with helium.

The constant stress imposed by the inner gas pressure in the tube walls is biaxial. Different levels of stress were achieved using several pressurized tube specimens. A summary of the dose and hoop stress levels experienced by the pressurized tubes studied is shown in Table 2.

The length and the diameter of the pressurized tubes are measured using a laser profilometry technique at room temperature on the outer surface. They were scanned three times axially with an axial step of 25 μ m and circumferentially, with a step of 45° for three positions along the axis of the tube (–10, 0 and + 10 nm). Diametrical profiles of the tube specimens were all not available, but the values of the length variation were all obtained. The measurements were performed in a hot cell by the research institute of atomic reactors (RIAR) near Dimitrovgrad after unloading of samples from BOR-60 at regular intervals.

All the small cylindrical tensile specimens were not placed within the same basket. For each irradiation cycle, they were not systematically in the same basket. Depending on the location of baskets and the irradiation cycle, the dose rate ranged from $\sim 7 \cdot 10^{-7}$ to $\sim 1 \cdot 10^{-6}$ dpa/s. The evolution of dose rate as a function of the rig length is relatively flat between Basket 1 and Basket 5. The maximum deviation was about 5%. For Basket 6 and Basket 7, the deviation from Basket 1 was less than 25%.

The shape of tensile specimen is indicated in Fig. 2 [50].

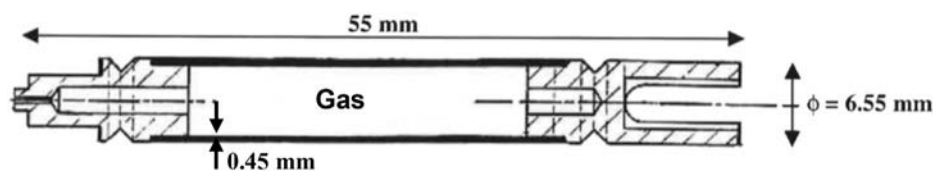
In order to better exclude specimen-to-specimen variability, the

Table 1

Metallurgical state, cold-working level, bulk composition (in wt%) and grain size of steel grades examined.

Material (heat)	Fe	C	Cr	Ni	Mo	Mn	Si	S	P	Cu	Co	Al	Ti	B	N	Grain size, μm
	Wt%													Wt ppm		
SA 304L (11922)	Bal	0.022	18.61	9.86	—	1.79	0.36	0.0007	0.032	0.25	0.06	—	—	9	610	30–40
SA 316 (32867)	Bal	0.054	16.60	10.60	2.25	1.12	0.68	0.022	0.027	0.24	0.12	—	<0.01	5	230	30–60
15% CW 316 (32867)																20–60
SA 316Ti (ESR 2992)	Bal	0.058	17.4	12.8	2.36	1.9	0.83	0.007	0.021	0.05	0.05	0.02	0.28	25	284	60
20% CW 316Ti (ESR 2992)																60–90
20% CW HP316 (EM613)	Bal	0.01	17.5	13.6	2.4	1.3	—	0.001	<0.001	—	—	—	—	—	10	20–30
20% CW HP316Si (EM614)	Bal	0.05	17.5	13.6	2.4	1.3	0.8	0.002	<0.001	—	—	—	—	—	10	20
SA N9 (HX3853/1)	Bal	0.068	11.68	25.74	1.74	1.82	0.76	0.002	0.008	—	—	0.009	0.51	65	45	40
21% CW N9 (HX3853/1)																60
SA 321 (93102)	Bal	0.059	17.9	10.1	0.24	1.67	0.51	0.013	0.027	—	—	—	0.59	18	9	90–130
SA NMF18 (ZA526)	Bal	0.123	17.6	0.45	0.17	18.6	0.53	0.001	0.025	0.1	—	—	—	—	5600	60–80

Note: For the grades available in both SA and CW states (316, 316Ti and N9 stainless steels), they were initially cold worked, then solution annealed by CEA.

**Fig. 1.** Pressurized tube for irradiation creep.**Table 2**

Hoop stress and dose levels of pressurized tubes studied.

Steel grade	Specimen reference	Hoop stress, MPa	Dose, dpa
SA 304L	A74	220	28.1, 41.2*, 51.6*, 69.3, 94.5, 119.9
	A79	150	
	A80	188	19.8, 32.8*, 43.2*, 60.9, 86.1
	A82	127	
	A110	188	22.3, 47.5, 72.9
	A109	127	22.3, 47.5
CW 316	B64	220	28.1, 41.2*, 51.6*, 69.3, 94.5, 119.9
	B65	150	
	B67	188	19.8, 32.8*, 43.2*, 60.9, 86.1
	B66	127	
	B121	127	22.3, 47.5, 72.9
	C5	188	24.5
SA 316			
CW N9	NB17	188	13, 23.5, 41.2, 66.4
	NB18	127	
CW HP 316	PB13	188	19.8
CW HP 316Si	PC13	188	19.8
	PC14	127	
CW 316Ti	K24	188	13*, 23.5*, 41.2, 66.4, 91.8
SA 316Ti	HT3	188	25.4
SA NMF18	VH13	188	25.4
SA 321	RB19	188	24.5

Note: Dose levels with (*) were obtained at the middle of two irradiation cycles. Creep behavior of the tubes with references in bold were studied by Garnier et al. [49].

tubes and tensile specimens came from the same heat: the tube wall, the end-cap and the tensile specimen underwent the same thermomechanical treatment (Table 1).

2.3. TEM examinations

After irradiation creep measurements, some gas-pressurized tubes (GPT) and some tensile specimens were used for TEM examinations (Table 3).

Slices were sectioned from the end-cap of the gas-pressurized

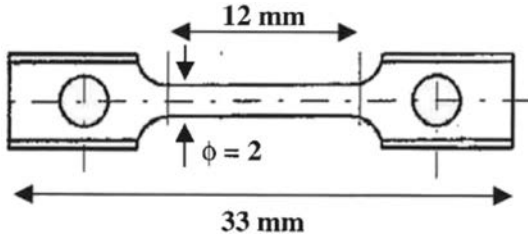


Fig. 2. Cylindrical specimen for tensile test.

images are detailed in previous studies [39e41]. Only precipitates which are located on the specimen edge were analyzed in order to avoid noticeable influence of the γ matrix.

Radiation-induced defect counting was performed by semi-automatic image analysis.

3. Results

3.1. Pressurized tube data

Table 3
Type of austenitic steel, shape of specimen, dose and stress level for the TEM foils studied.

Materials	Basket	Shape of specimen	Specimen reference	Dose, dpa	Hoop stress level, MPa
SA 304L	1	GPT	A80	~86	0
			A74	~120	188
SA 316 15% CW 316	1	GPT	C5	~25	188
		GPT	B67	~86	0
20% CW 316Ti	1	GPT	K24	~91	188
20% CW HP316	5	TS	PB5	19.6	0
	1	GPT	PB13	~20	188
20% CW HP316Si	5	TS	PC9	19.6	0
	1	GPT	PC13	~20	188
20% CW 316Ti	5	TS	K37	20.6	0
	5 and then 2		K33	40	0
SA 316Ti	5	TS	H11	20.6	0
	5 and then 7		H7	35.2	0
SA N9	6	TS	NB41	17.7	0
SA 321	6	TS	RB1	17.5	0
SA NMF18	2	TS	VH1	19.5	0

tubes and the head of the tensile specimens for unstressed conditions (0 MPa) and from the wall of the gas-pressurized tubes for stressed conditions (188e220 MPa).

All slices were mechanically thinned down to about 100 μm . 3-mm disks were punched from these slices and thinned using a Tenupol-5 twin-jet electropolisher.

Microstructural examinations were performed using a JEOL 2010 field-emission-gun TEM and a JEOL 2100 LaB₆ TEM both operating at 200 kV. The used techniques were conventional bright field- and dark field-TEM (CBF- and CDF-TEM) imaging and electron diffraction. The studied zone axes of the γ matrix were of type $\langle 001 \rangle$, $\langle 011 \rangle$ and $\langle 111 \rangle$.

The second microscope is equipped with a GATAN imaging filter (GIF Tridiem) for performing thickness measurements using electron energy loss spectroscopy (EELS) and chemical analyzes using energy filtered imaging (EF-TEM).

Thickness measurements performed on some TEM foils have shown that the investigated areas can have a thickness value ranging from 70 to 150 nm. In practice, the CBF- and CDF-TEM images acquired in several different perforation zones of TEM foils for obtaining a better statistic of each type of defects are often too numerous to allow thickness measurements to be carried out systematically. Moreover, in order to minimize variations in thickness, the specimen holder was not strongly tilted. Thereby, the best way to compare concentration of radiation defects between various steel grades is to present the results of density of these defects with an error bar to take into account the thickness variation.

EF-TEM imaging was used to identify the chemical species present in precipitates. The methods of acquisition of EF-TEM

Fig. 3 shows the results of CW N9 tubes irradiated up to ~66 dpa with hoop stresses of 127e188 MPa and of CW 316Ti tube irradiated up to 91 dpa with a hoop stress of 188 MPa. Note that no comparable specimen is available at 0 MPa. The evolution of the outer diametrical strain of tubes as a function of dose is linear. The strain rate increases with increasing stress level. Note that in low dose region, the 0 dpa intercept of the linear fit is negative. There is a

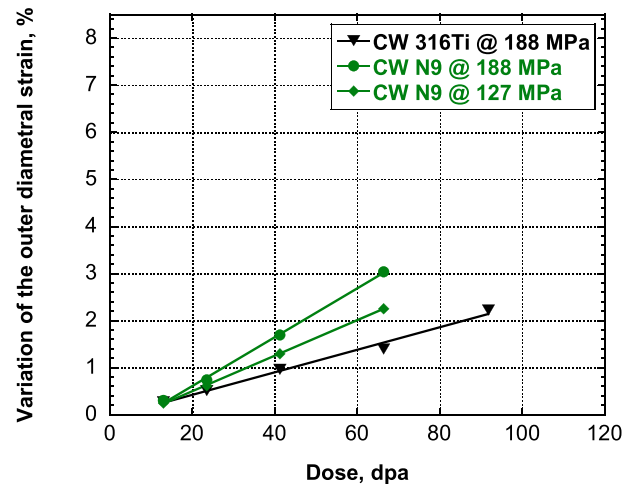


Fig. 3. Evolution of in-reactor creep as a function of dose for CW N9 and CW 316Ti at different stress levels.

threshold dose, about a few dpa, above which the variation of strain is positive. In the case of CW N9, a stress dependence of threshold dose is observed. The higher the stress level is, the lower the threshold dose level is.

Fig. 4 shows the variation in diameter of CW 316Ti, CW N9, CW HP316, CW HP316Si, CW NMF18, SA 321, SA 316 and SA 316Ti as a function of hoop stress and dose levels. Note that a single measurement was performed for some grades, namely CW HP316, SA 316, SA 316Ti, SA 321 and SA NMF 18, and two measurements for CW HP316Si. The results obtained in CW N9 and CW 316Ti confirmed the linear variation in diametrical strain as a function of stress \times dose reported in Ref. [49].

From the limited available data, a threshold above which the diametrical variation is positive appears to occur at higher stress \times dose levels for CW 316, SA 304L and CW N9 than for CW 316Ti.

No significant variations in the length of the tubes were noticed: the measured values were found to be relatively scattered in the very small range [-0.54, 0.3] in percent. These results suggest that swelling is nil or negligible in the conditions of temperature, dose rate and neutron spectrum used in this study. Otherwise, this hypothesis is validated by TEM observations (see in section 3.2.): no cavities were observed.

In light of the results, the effective strain of irradiation creep can be described by the following equation [49]:

$$\bar{\epsilon} = B_0(\bar{\sigma}ft - B_1)$$

where $\bar{\sigma}$ and $\bar{\epsilon}$ are respectively the effective Von Mises stress and the effective strain. B_0 is the swelling independent steady-state irradiation creep compliance, B_1 corresponds to the threshold stress \times dose for steady-state irradiation creep, f the flux and t the duration of irradiation. For a thin-walled tube, the effective stress $\bar{\sigma}$ is equal to the hoop stress $\bar{\sigma}_q$ multiplied by a factor of $\sqrt{3}/2$ and the effective strain $\bar{\epsilon}$ to the tangential strain ϵ_q multiplied by a factor of $2/\sqrt{3}$. In order to calculate B_0 in the standard manner for comparison with literature values, a mid-wall correction was made. This correction consists in using the average diameter of the tube D^{av} instead of the external diameter D^{ext} with $D^{av} = (D^{ext} + D^{in})/2$. The diametrical strain ϵ_q is estimated by the average diameter variation $\epsilon_q = DD^{av}/D_0^{av}$. Since the inner diameter (and the thickness) cannot be measured after creep irradiation, it has been estimated on the principle of conservation of volume. The details of formulas and equations are given in Appendix.

The values of the irradiation creep coefficients of the steel grades studied is shown in Table 4. The compliance value of CW N9 is higher than that obtained in SA 304L. CW 316Ti has the lowest value of compliance. The value of CW 316 is intermediate between those of SA 304L and CW 316Ti and is in good agreement with the values obtained by Grossbeck et al. and Foster et al. after irradiation at 330 °C [15,16]. The irradiation creep threshold is about 800 MPa dpa, except for that of CW 316Ti which is about 380 MPa dpa.

As to the other steel grades for which there are fewer experimental points, the value of irradiation creep threshold may be between 0 and over 800 MPa dpa. Therefore, one can expect to a possible large scatter of compliance values. Values can exceed that indicated in Table 4. For the same chemical composition, it is not clear whether SA steels have a smaller incubation threshold than CW steels or not (SA 316Ti versus CW 316Ti and SA 316 versus CW 316).

As already shown by Garnier et al. [49], the steady-state irradiation creep rate of SA 304L is significantly higher than that of CW 316. Based on the fact that SA 316 has a threshold value superior or equal to 0 and thus a higher rate than CW 316, the difference of rate is assumed to be due mainly to the initial thermo-mechanical treatment (cold-working). This effect of the initial thermo-mechanical treatment is more apparent concerning 316Ti. The creep rate of CW 316Ti is slightly lower than that observed in CW 316, indicating that a higher cold working level possibly induces a decrease in creep rate (20% for CW 316Ti and 15% for CW 316).

If SA 316, SA 316Ti and SA 304L really have the same creep rate, the small difference of concentration of the major and minor alloying elements should have no significant effect on this rate.

Although initially cold-worked, N9 has a similar behavior to SA 304L, indicating a possible effect of concentration in major elements as Cr and Ni on creep rate (12%Cr and ~26%Ni for N9 instead of 17e19%Cr and 10e11%Ni for 304L and 316).

Although solution-annealed, NMF18 has the lowest variation in

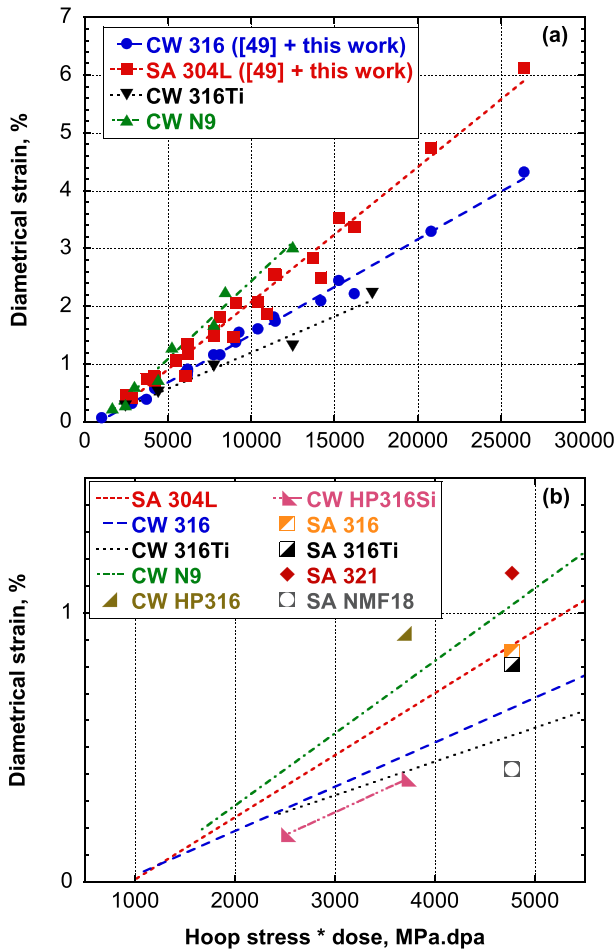


Fig. 4. Variation in diametrical strain as a function of stress and dose for (a) SA 304L, CW 316, CW 316Ti and CW N9 (experimental points and strain linear fits (represented by the dashed lines)) and for (b) all the steel grades. In (b), for more clarity, the experimental points of SA 304L, CW 316, CW 316Ti and CW N9 were removed.

Table 4

Irradiation creep coefficients of different austenitic steel grades at steady state. In the frame of the present study, data from specimens detailed in Ref. [49] (and completed in this study) have been reprocessed, leading to new values for B_0 and B_1 .

Austenitic steel grades	$B_0, 10^{-6} \text{ MPa}^{-1} \text{ dpa}^{-1}$	$B_1, \text{ MPa dpa}$
SA 304L	3.55	811
CW 316	2.55	729
CW 316Ti	1.97	379
CW N9	4.15	827

diameter. To date, in the absence of the threshold value, the effect of manganese, instead of nickel, on decreasing of creep rate of austenitic steel could not be examined.

Whatever the value of its incubation threshold, SA 321 creeps faster than SA 304L. These two types of steel have similar chemical compositions. The grain size was found to be relatively high compared to the other steel grades. Therefore, a higher grain size possibly induces an increasing of creep rate.

As to CW HP316 whose variation in diameter is significantly higher than that of CW 316, it is likely that CW HP316 creeps faster than CW 316. Without exactly knowing the threshold value of CW HP316Si, this latter steel (on the basis of only two results) tends to exhibit the same creep rate as CW 316. The comparison of creep rate between CW HP316Si, CW HP316 and CW 316 is not easy to draw reliable conclusions on the effect of minor alloying elements (or impurities) on creep rate of CW 316. Indeed, CW HP316, CW HP316Si and CW 316 have different chemical compositions in terms of contents of major and minor alloying elements (Cr, Ni, Cu, Co, Al, B and N). These different contents prevent to investigate the impact of silicon and carbon on possible decrease of creep rate of CW 316.

To summarize, the parameters, which make it possible to improve the steady-state irradiation creep resistance of austenitic steel, have been identified. Cold-worked structure, noticeable decrease of Ni content (at least, between 0.5 and 26%) and perhaps decrease of grain size tend to decrease its steady-state irradiation creep rate. These effects are visible especially at high dose and stress levels.

3.2. TEM observations

Frank-faulted loops and dislocation lines were all present in the microstructure of the different austenitic steels irradiated between 17.5 and 120 dpa at 320 °C with and without hoop stress. Depending on the grade of steels, precipitates were finely produced by irradiation. They could be abundant. No cavities were detectable. As to twins, they were present in CW specimens and also in highly irradiated SA 304L with a stress of 220 MPa. The irradiated microstructure can be also characterized by a high density of possible "black dots". This other microstructural component is commonly called defect clusters and is too small to resolve in TEM (Typically, ϵ 2–4 nm). Black dots are especially taken into consideration at low temperatures (below 300 °C) at which no precipitates are detectable and fairly large Frank loops or stacking fault tetrahedrons (SFT) exist in a small amount. Frank loops, SFTs and sometimes precipitates have characteristic shapes. These shapes are distinguishable if the defects are well separated from each other. In the present study, i.e. with highly irradiated steels, Frank loops, perfect dislocations and sometimes precipitates were found to be very close to each other. The shape of very fragmented dislocation lines, small Frank loops and precipitates could lead to the same contrast as black dots. For these reasons, bright field images (black dots) and even weak beam dark field images (white dots) were of little use to examine the possible black dots and thus to determine their number density or size with a high accuracy.

3.2.1. Twins

Twins formed by the initial cold-work are unaffected by irradiation and hoop stress (Fig. 5).

Isolated nanotwins were observed especially in rare grains of SA 304L irradiated under a hoop stress of 220 MPa. It may be due to the high level of applied stress. Prior to irradiation and at 320 °C, the yield stress appears to be about 210 MPa [50].

3.2.2. Frank loop structure

{111} $_{\gamma}$ -faulted dislocation loops, i.e., Frank loops, were present in

all the irradiated steel grades regardless of their metallurgical state and the level of hoop stress applied under irradiation. The loops produce distinctive satellite spots around the matrix reflections. These satellite spots arise from extended diffraction streaks (reciprocal lattice rods (relrods)) perpendicular to the four sets of {111} $_{\gamma}$ planes. As shown in Fig. 6, the CDF-TEM images taken with one of the $\langle 111 \rangle_{\gamma}$ relrods revealed one Frank loop variant. The four sets of $\langle 111 \rangle_{\gamma}$ diffraction streaks are visible in two-beam conditions [9,39].

There are different ways to visualize the distribution of Frank loops in the four sets of {111} $_{\gamma}$ planes inside the same grain of steel without having to tilt this grain to get access to each of these sets in CDF-TEM imaging [9,38,39,51]. In this condition, a similar thickness of the foil is seen for the four Frank loop variants. This is the case in this study where the four satellite spots in the [001] diffraction pattern were selected to visualize the Frank loops.

At unstressed conditions, the Frank loop density, mean size, and size range for each austenitic steel grade are displayed in Figs. 7 and 8. Almost the same order of magnitude for the Frank loop density of the different grades can be noticed at a dose of ~20 dpa. Based on a single dose value, no firm conclusion can be drawn as to the possible effect of chemical composition and metallurgical state on the Frank loop density. At higher dose levels, SA and CW 316Ti, SA 304L and CW 316 revealed a similar value of the Frank loop density (Fig. 8(a)). Significant differences are mainly reported for higher irradiation temperatures, for several doses and for SA 304L, SA 316 and CW 316 [41].

Whatever the dose value, no notable differences occur in the Frank loop mean size and size range, except in the maximal size, which is twice as high in SA NMF18 and CW HP316 as in the other grades (Figs. 7 and 8(b)). In CDF-TEM imaging, the loop detection limit is about 2 nm. No minimal loop size beyond 2–3 nm was observed.

Although the unstressed materials were not all in the same basket, the loop density and mean size observed in these materials cover a similar range of density and size, respectively. This means that at least at ~320 °C, the dose rate range studied had no significant effect on the loop microstructure. The values of the Frank loop density and mean size are similar to that obtained by Yang et al. [42,52] who examined different steel grades such as SA 304, SA HP304L, SA 304-low S, SA 304-high S, SA 316-low C, high N, These steels were irradiated up to 25 dpa at 320 °C in BOR-60.

As shown in Fig. 9, no anisotropy of the loop distribution in {111} $_{\gamma}$ planes was observed, for example in unstressed SA 304L. In other words, the Frank loop density and size are similar in the four sets of {111} $_{\gamma}$ planes.

With a hoop stress of 188 MPa applied under irradiation in SA 304L, SA 316, CW HP316 and CW HP316Si, no notable partitioning of Frank loops occurs except for CW HP316 for both the density and mean size and CW HP316Si notably for the mean size. The corresponding distribution of Frank loops in the four sets of {111} $_{\gamma}$ planes of each grain in terms of density and mean size is shown in Figs. 9 and 10. In CW HP316, the fraction of total loop population on the four sets of {111} $_{\gamma}$ planes is respectively 40.3, 39.9, 13.9 and 7%.

The total density of Frank loops is lower with a stress applied under irradiation than without stress. The opposite effect is observed in size.

It is noted here that it was not possible to obtain images arising from $\langle 001 \rangle_{\gamma}$ zone axis of SA 304L irradiated with a stress of 220 MPa and CW 316 and CW 316Ti irradiated with a stress of 188 MPa in the thickness of interest. Therefore, for these specimens, the possible partitioning of Frank loops between the different planes could not be examined. Nevertheless, the same tendency for the stress effect on density and size is noticed with dark-field images obtained using the relrod near the $\langle 002 \rangle_{\gamma}$ reflection in the following condition

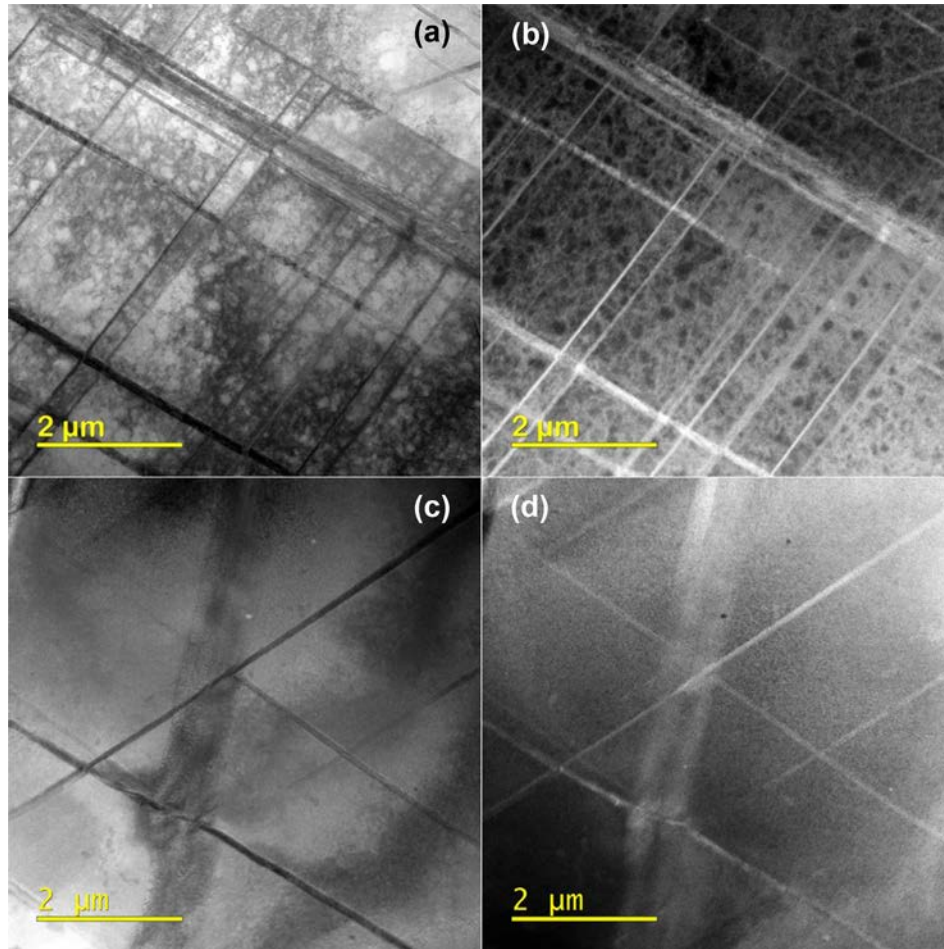


Fig. 5. Twins in CW HP316Si (a,b) before and (c,d) after irradiation to ~20 dpa with a hoop stress of 188 MPa. On the left, STEM-BF images and on the right, STEM-HAADF.

$\mathbf{B} \sim [110]_{\gamma}$, $\mathbf{g} = [1-13]_{\gamma}$.

Fig. 11 illustrates the dose dependence of Frank loop characteristics observed in SA 304L, CW 316, CW 316Ti, CW HP316, CW HP316Si and SA 316, with and without stress. The results obtained from the unstressed specimens were published in previous studies [29,37,38]. The values of the loop density are given for an assumed thickness of the foil of 100 nm. Without stress applied under irradiation, the value of the Frank loop density per $\{111\}_{\gamma}$ plane increases notably at low doses. It is the same for the mean loop size. Above around 10 dpa, the microstructure of Frank loops approaches a quasi-equilibrium state or a steady state. For all the grades but CW 316Ti, the mechanical stress applied under irradiation induces a decrease of the Frank loop density and an increase of their size, compared to those measured after irradiation without stress. According to the steel grades, the decrease factor of density varies from 2.3 to 5.7.

3.2.3. Dislocation lines

Fig. 12 shows a dense population of dislocation line segments throughout the γ matrix of CW 316Ti, in $\mathbf{g} \approx [1-11]_{\gamma}$ contrast near a $(110)_{\gamma}$ foil. Unlike dislocation lines induced to higher neutron-irradiation temperatures (>450 °C), they seem to be very close to each other. The image of dislocations was taken in a low thickness, typically 10–50 nm (measured from thickness map in EF-TEM), which enables to restrict the contrast of the strain fields induced by Frank loops, perfect dislocations, and precipitates.

In the thickness of interest usually used to image each type of

radiation defects on the case-by-case basis, the strain fields from numerous Frank loops, perfect dislocations, and precipitates overwhelm the microstructure contrast in CBF imaging condition. Their tiny distance often makes perfect dislocations barely visible, even sometimes with a weak-beam dark-field image.

The dislocation microstructure observed in stressed and unstressed irradiated specimens is very different from the initial dislocation network with dislocation cells, as observed in unirradiated CW austenitic steel (Fig. 5). The dislocation segments seem to correspond to those formed from the accumulation of radiation-induced defects rather than the direct remnants of the CW dislocation structure. The perfect dislocation microstructure changes during irradiation from one containing a dislocation cell structure for CW steel grades and some dislocations widely dispersed for SA steel grades to one apparently containing a dense homogeneous spatial distribution of dislocation segments.

After irradiation, the dislocation density is roughly superior to 1.10^{15} m^{-2} in the condition $\mathbf{B} = [110]_{\gamma}$, $\mathbf{g} \approx [1-11]_{\gamma}$. As dislocation segments were found to be not all distinguishable, leading to scattered data, it was not possible to examine the evolution of dislocation density as a function of dose with and without stress for each steel grade.

3.2.4. Precipitates

Precipitates can be visualized using CDF-TEM, high contrast Moiré fringe (if there is a lattice mismatch with respect to the γ matrix) or EF-TEM imaging (Figs. 13–16).

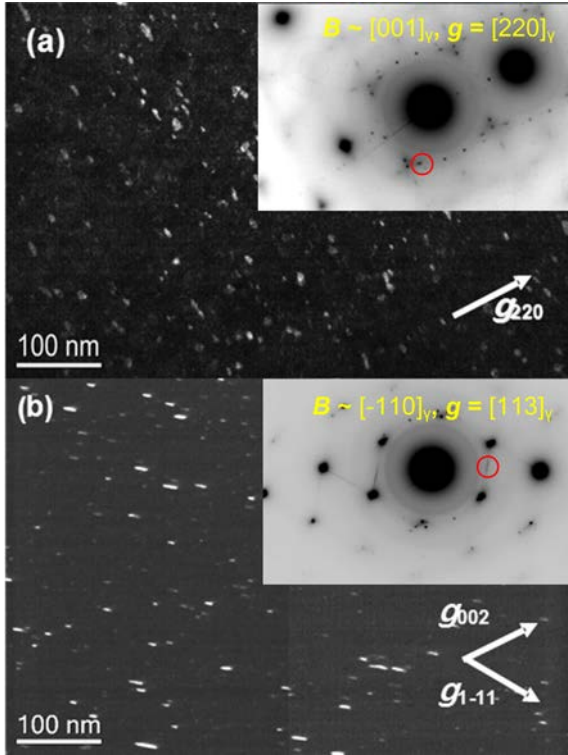


Fig. 6. CDF-TEM images of (a) inclined and (b) edge-on Frank loops observed in SA 304L irradiated up to 86 dpa with a hoop stress of 188 MPa. Corresponding diffraction patterns are shown as insets. One of the four $(111)_\gamma$ reldors for imaging of one variant of Frank loops is indicated by red circle. (For interpretation of the references to color in this figure legend, the reader is referred to the web version of this article.)

As shown in Fig. 13(a), the relative position of reflection spots of precipitates compared to the γ matrix of irradiated SA N9 is consistent with the existence of the Ni_3Si (γ')-type precipitates. The γ' precipitates adopt ordered variations of the face-centered cube (FCC) lattice and have a cube-on-cube orientation relationship with the γ matrix [53e56]. Their superlattice reflection spots have been indexed with respect to the matrix reflection spots. In Table 5, the values of the a_0 lattice parameters are given as measured on the SAD pattern. These values agree well with reference powder diffraction data for both γ' and γ . The γ' precipitates are nano-sized and irregular-shaped particles (Fig. 13(b)). Their spatial distribution is homogeneous.

No visible γ' precipitates were found in other grades. However, precipitates with a high lattice mismatch with respect to the γ matrix were observed in those other grades.

Reflection spots of precipitates in SAD patterns can be invisible, mainly for weakly irradiated specimens. In zone axis, that is to say in many/multi-beam condition, diffraction occurs for all the reciprocal lattice points lying close to the Ewald sphere (Fig. 14(a,b,c)). However, those points are not as intense as the central $[000]$ beam since the former points do not lie exactly on the Ewald sphere. Two-beam condition brings a particular reciprocal lattice vector $\mathbf{g}_{(hkl)}$ exactly on this sphere. This makes particular matrix reflection as intense as the central beam. This is particularly useful for highlighting the precipitate reflection spots of low intensity located between these transmitted and diffracted spots (Fig. 14(d)). The intensity of other reflection spots of the γ matrix is low because these spots are far away from the Ewald sphere.

With increasing doses and regardless of steel grades, precipitate reflection spots become more visible in two-beam/multi-beam conditions.

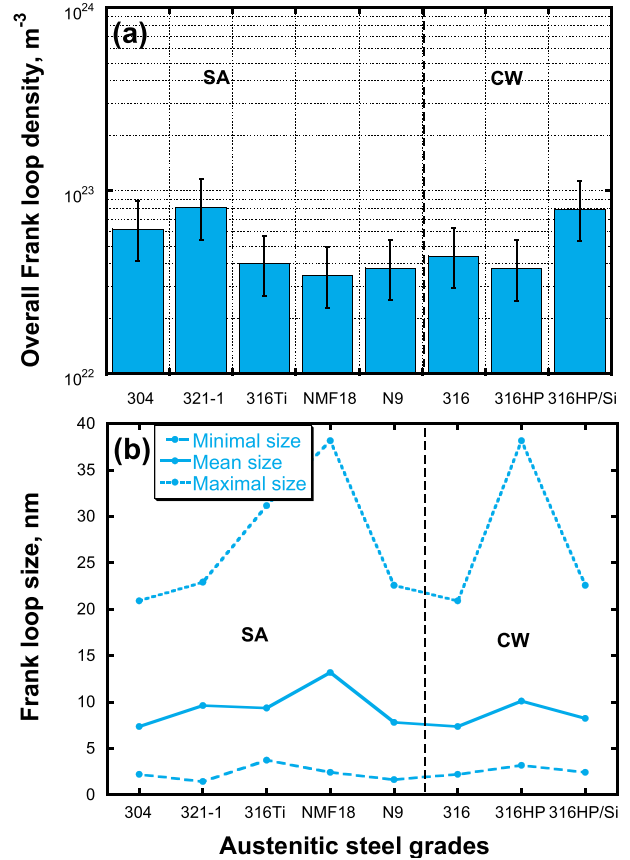


Fig. 7. (a) Density, (b) mean size, and range size of Frank loops for the different steel grades at a dose of about 20 dpa without stress. Here, the overall density corresponds to one Frank loop variant multiplied by four to account for all of the possible Frank loop variants. The results of SA 304L and CW 316 were yielded in Ref. [29].

SAD patterns clearly reveal reflection spots from an FCC lattice. A cube-on-cube orientation relationship ($[100]_{\text{ppt}} \parallel [100]_\gamma$, $(010)_{\text{ppt}} \parallel (010)_\gamma$) between the γ matrix and the precipitates (Fig. 14(a,b,c,d)) was found. The reflections of the form $\{00l\}$, with odd numbers in l , are forbidden. Their precipitate reflection spots have been indexed with respect to the γ matrix lattice. The $d_{(hkl)}$ -spacings for the precipitate were measured and the corresponding lattice parameters are provided in Table 5. The precipitate lattice parameter appears to be slightly greater than three times that of the γ matrix.

There are three known precipitate phase which have structures which may be interpreted as face-centered cubic [54,57,58]: τ (M_{23}X_6 , where M is a transition element and X = C, Si ...) carbides, η (M_6X) carbides or G ($\text{M}_6\text{Ni}_{16}\text{Si}_7$)-silicides. The values of the a_0 lattice parameters measured on the basis of SAD patterns are listed with reference powder diffraction data for γ , τ , η and G (Table 5). A good agreement between the reference and experimental data for the γ matrix is noted. As to the precipitates, best fit seems to be achieved for the τ carbides, however the G-phase is also probable. The η carbides have a space group $Fd-3m$, i.e. a diamond cubic structure, instead of $Fm3m$ for the other two types of precipitates. However, no missing or weak spots, i.e. $\{200\}$ or $\{420\}$, in SAD from the η carbides were found. Otherwise, these missing spots could be masked by non-zero intensity spots from other types of precipitates.

Furthermore, the G phase has already been observed in low-nickel austenitic stainless steels during neutron irradiation at very low dose rates [36]. In these steels, it was found that the nanometric G-phase precipitates have a lattice parameter slightly

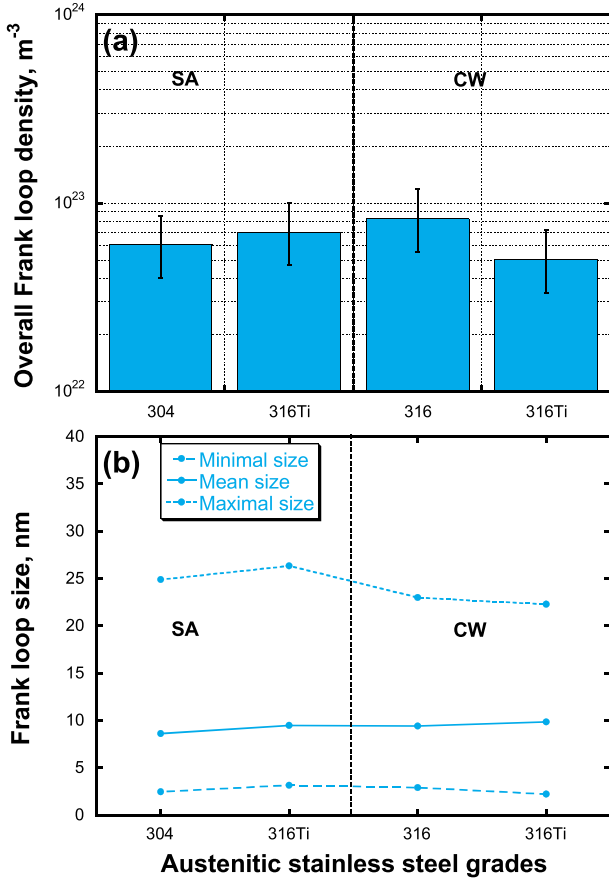


Fig. 8. Frank loop (a) density, (b) mean size and size range for the different steel grades at a dose of 35×10^{20} dpa without stress. Here, the overall density corresponds to one Frank loop variant multiplied by four to account for all of the possible Frank loop variants. The results of SA 304L and CW 316 were yielded in Ref. [29].

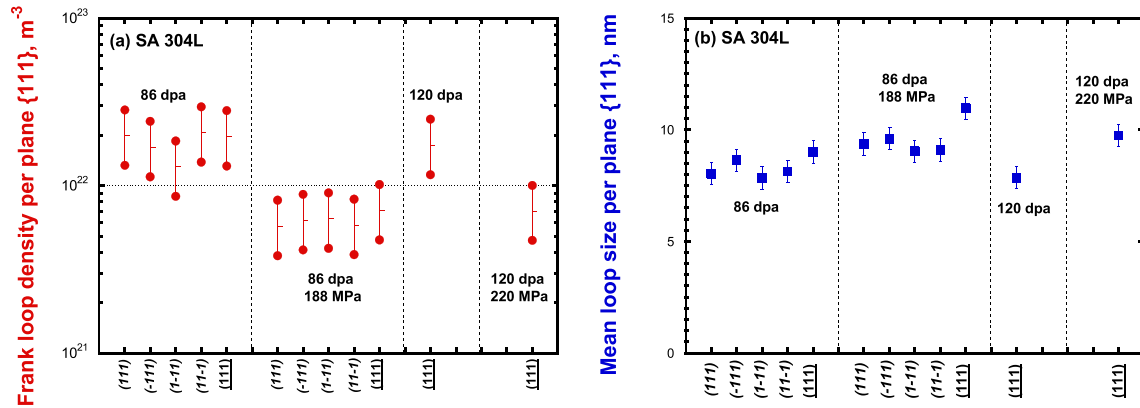


Fig. 9. (a) Density and (b) mean size of Frank loops per $\{111\}_\gamma$ plane observed in SA 304L irradiated up to high doses with and without a stress ranging from 188 to 220 MPa. Each $\{111\}_\gamma$ plane in italic corresponds to each satellite spot in the following conditions $\mathbf{B} \sim [001]_\gamma$, $\mathbf{g} = [220]_\gamma$. The underlined $(111)_\gamma$ plane corresponds to the extended streak visible around the $(002)_\gamma$ reflection in the following conditions $\mathbf{B} \sim [-110]_\gamma$, $\mathbf{g} = [113]_\gamma$.

smaller than that of classical G-phase precipitates [59e63]. Unfortunately, the value of their lattice parameter, and the nature of the specific orientation relationship between the matrix and these precipitates have not been provided. Williams [57] reported that the G-phase particles observed in irradiated FV548 steel had a parallel orientation relationship with the γ matrix.

Fig. 14(e) shows the presence of many nanoscale precipitates in CDF-TEM imaging after placing a small objective aperture around

the reflection spot positioned at $\sim 2/3$ from the distance between $(000)_\gamma$ and $(-220)_\gamma$ under $\mathbf{B} \sim [110]_\gamma$ and $\mathbf{g} = [-220]_\gamma$. Even if precipitate reflection spots are not visible and despite the use of two-beam conditions, it is sometimes possible to visualize precipitates in CDF-TEM imaging condition by placing a small objective aperture in blind at their theoretical position. Here, this position is located at $2/3$ from the distance between $(000)_\gamma$ and $(-220)_\gamma$. The precipitates are in the form of nano-sized and round/oval-shaped platelets (Fig. 14(e)). Their spatial distribution is homogeneous.

In highly irradiated specimens of SA 304L and CW 316Ti (≥ 91 dpa), SAD patterns, in particular around $\langle 001 \rangle_\gamma$ zone axis, reveal additional precipitate reflection spots (Fig. 14(b,c)). Further studies are needed to determine the number of possible crystallographic phases or variants. Based on the results obtained from EF-TEM images (see below, Fig. 16), there might be several variants.

Small precipitates of high lattice mismatch with respect to the γ matrix can also be studied using high contrast Moiré fringe imaging (Fig. 14(f)). Here, the lattice fringes in the following condition $\mathbf{B} \sim [110]_\gamma$ and $\mathbf{g} = [002]_\gamma$ are almost parallel Moiré fringes. Indeed, each precipitate has a Moiré fringe that is almost aligned with the $\{002\}_\gamma$ planes. This indicates that precipitate reflection spot in the diffraction pattern is close to that of the γ matrix. They clearly appear if the precipitate size is twice as high as the spacing of Moiré fringes. Fig. 15 illustrates that at low doses, all Moiré fringes are not visible if the precipitate mean size is inferior or equal to 5 nm. On the contrary, CDF-TEM imaging allows us to visualize the smaller precipitates. The precipitates appear as nano-sized and round/oval-shaped platelets and are distributed homogeneously.

The value of the $d_{(hkl)}$ -spacing given from the Moiré fringe spacing $D = 18 \times 10^{-22} \pm 1$ Å and $d_{002}^{\text{matrix}} = 1.8$ Å in the following condition $\mathbf{B} \sim [110]_\gamma$ and $\mathbf{g} = [002]_\gamma$ is about 1.66×1.68 Å. Among the precipitates identified in austenitic steels irradiated at higher temperature, this calculated value may correspond to the reticular distance d_{600} of η carbides (Powder Diffraction File (PDF) N°04-008-9162). It is however not excluded that it may also be τ carbides

(PDF N°04-007-1216) or G-phase (PDF N°04-001-5050).

The EF-TEM images taken with the three-window method for three major chemical elements in CW 316Ti irradiated to around 91 dpa without stress are shown in Fig. 16. In the Fe $L_{2,3}$ and Cr $L_{2,3}$ elemental maps, numerous nano-sized and round/oval-shaped regions are clearly visible (Fig. 16(a,b)). These regions are depleted in Fe and Cr relative to the γ matrix chemical composition. When compared to the Ni $L_{2,3}$ elemental map shown in Fig. 16(c),

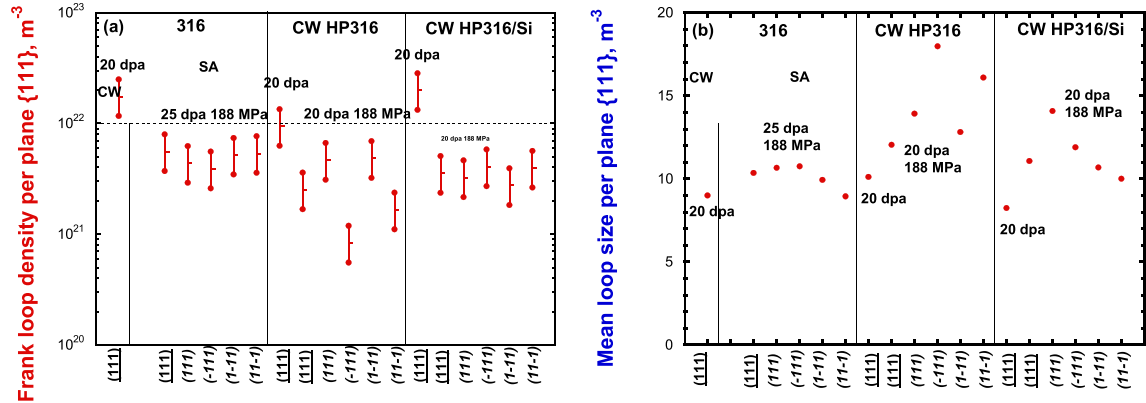


Fig. 10. (a) Density and (b) mean size of Frank loops per $\{111\}_\gamma$ plane observed in various stainless steels irradiated up to 20×10^{25} dpa with or without a stress of 188 MPa. Each $\{111\}_\gamma$ plane in italic corresponds to each satellite spot in the following conditions $B \sim [001]_\gamma, g = [220]_\gamma$. The underlined $\{111\}_\gamma$ plane corresponds to the extended streak visible around the $(002)_\gamma$ reflection in the following conditions $B \sim [-110]_\gamma, g = [113]_\gamma$.

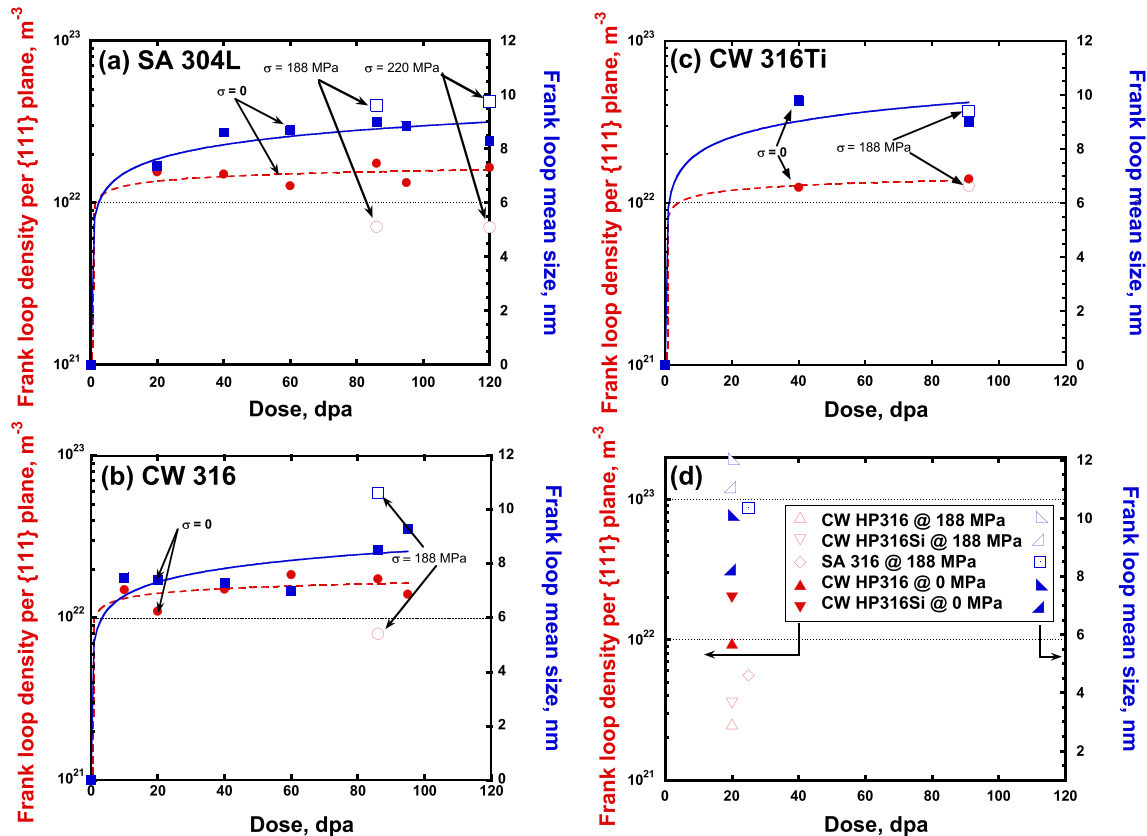


Fig. 11. Evolution of the Frank loop density (dashed lines) and mean size (continuous lines) in (a) SA 304L, (b) CW 316, (c) CW 316Ti, (d) CW HP316, CW HP316Si and SA 316 as a function of dose with (open dots) and without (filled dots) a stress ranging from 188 to 220 MPa [29,37,38].

the regions depleted in Fe and Cr correlate well with Ni enrichment. There is a single type of precipitates. Their size of about 8 nm and their morphology/shape are similar to those provided by CDF-TEM and Moiré fringe imaging.

The results of Energy Dispersive Spectroscopy (EDS) analysis obtained from the various precipitates observed in 300-series austenitic stainless steels after irradiation at higher temperature revealed that η carbides are typically rich in nickel, chromium, and silicon and can contain iron, and that τ carbides are mainly rich in chromium with a low solubility for nickel and silicon. In this work, the absence of Cr enrichment excludes the presence of τ carbides.

By comparison with EDS spectra obtained in G particles, which show a high concentration of nickel and silicon, and a nonzero concentration of manganese, iron, molybdenum and even sometimes Fe and Cr, the nickel-rich precipitates could also match with G-phase [63,64]. Therefore, on the basis of these chemical investigations obtained up to now, the small platelets are classified as η carbides or G phase. Their clear differentiation is only possible when using EELS and EF-TEM imaging with a detection of carbon, silicon and manganese at the nanoscale. Nevertheless, due to the low concentration of these chemical elements, less than about 2% wt, their detection was often difficult using these methods. The C K

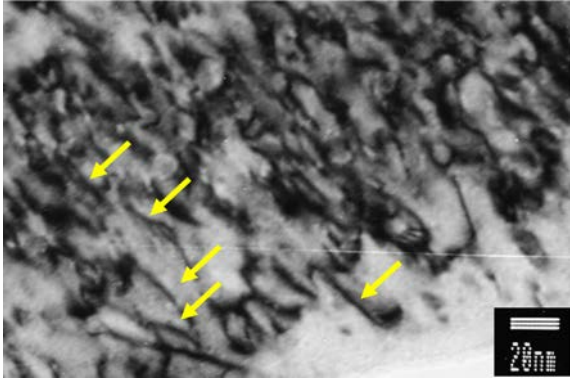


Fig. 12. Dislocation lines near a bend fringe in CW 316Ti irradiated up to -91 dpa under a hoop stress of 188 MPa. $B \sim [110]_{\gamma}$, $g \sim [1\bar{e}11]_{\gamma}$.

precipitates that have a lattice mismatch with respect to the γ matrix.

From a quantitative point of view, the precipitate density and size are respectively of order of $10^{20}e7 \times 10^{21} m^{-3}$ and $6e7$ nm in SA 304L, SA 316Ti, CW 316 and CW 316Ti (Table 6). No fine precipitation could be noticed in SA NMF18, SA 321, CW HP316 and CW HP316Si. As to SA N9 grade, the indefinite shape of precipitates, with the bottom of images which was not very dark, did not allow them to be quantified.

The evolution of the precipitate density and size in SA 304L, CW 316, CW 316Ti, CW HP316, CW HP316Si and SA 316 as a function of dose with and without stress is plotted in Fig. 17. The results obtained from the head of the tensile specimens irradiated at doses different from those shown in Table 3 were published in previous studies [37,38].

Without stress applied under irradiation, precipitation is

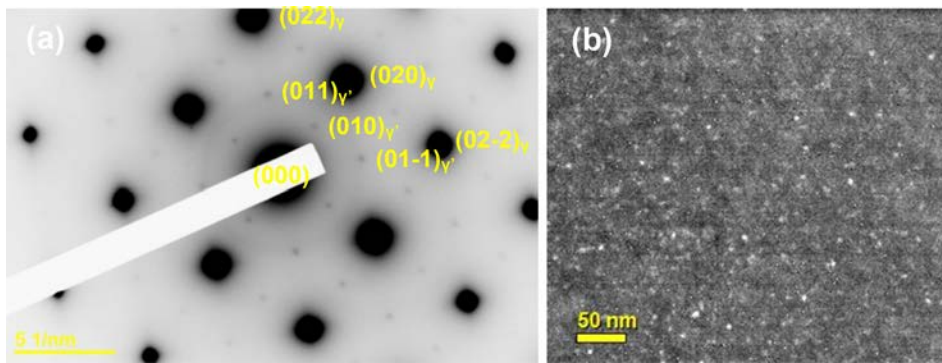


Fig. 13. SA N9 irradiated up to 17.7 dpa without stress. (a) SAD pattern taken with $B = [100]_{\gamma}$, (b) CDF-TEM image taken from the $(-110)_{\gamma}$ reflection spot in the condition $B = [110]_{\gamma}$, $g = [-220]_{\gamma}$.

Table 5

Mean values of lattice parameter for the γ matrix and different precipitates. According to the corresponding Miller indices, the lattice parameter of precipitates in CW 316Ti can vary from 10.1 to 11.25 Å.

Measurement by TEM		Powder Diffraction File
$a_0, \text{Å}$		
γ matrix (FCC Fm3m) of SA N9	γ matrix (FCC Fm3m) of CW 316Ti	No. 00-47-1417 (Fe, Ni)
3.54	3.62	3.6
Precipitates (FCC) in SA N9		No. 00-006-0690 (γ')
3.54		3.5
	Precipitates (FCC) in CW 316Ti	No. 04-007-1216 ($Cr_{23}C_6$) / 04-008-9162 (CCr_3Ni_2Si) / 04-001-5050 ($Cr_3Mn_3Ni_{16}Si_7$)
	10.66	10.76 / 10.93 / 11.09

signal is near the detection limit and may also be due to carbon contamination during investigation. Mn $L_{2,3}$ elemental map is hard to obtain because of overlapping closely adjacent Cr $L_{2,3}$ (575 eV) and Mn $L_{2,3}$ (641 eV) edges. Especially with the precipitates in the form of thin platelets, Si enrichment or depletion is hard to detect.

The results obtained by CDF-TEM, Moiré fringe and EF-TEM combined imaging, even if giving lot of information, reveal that further investigations are needed to identify the precipitates. By comparison with the results obtained by Refs. [60,62], it may be the G-phase precipitates with a lattice parameter smaller than that of classical G-phase precipitates. Anyways, there are many

intense in CW 316 whereas it increases extensively in SA 304L notably in terms of density. As to the precipitate size, it increases gradually.

With stress, the precipitate density and size increase mainly in SA 304L and CW HP316Si grades. No precipitates could be found in CW HP316. With the same size around 20 dpa, the precipitate density is an order of magnitude lower in CW HP316Si irradiated with stress than SA 304L, CW 316 and CW 316Ti irradiated without stress.

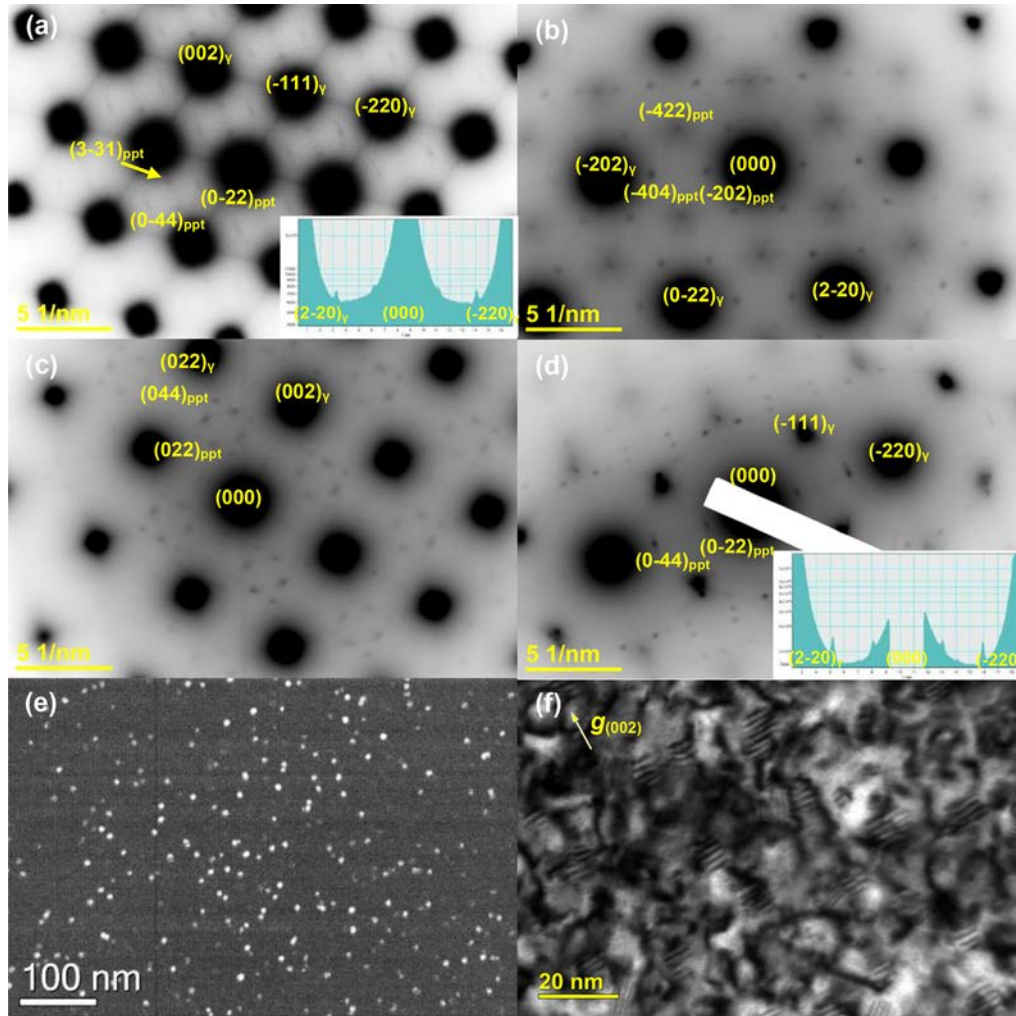


Fig. 14. CW 316Ti irradiated up to ~91 dpa under a stress of 188 MPa. Indexed (a) $[011]_{\gamma}$, (b) $[111]_{\gamma}$ and (c) $[001]_{\gamma}$ SAD patterns. (d) SAD patterns with the condition $\mathbf{B} \sim [011]_{\gamma}$, $\mathbf{g} = [02-2]_{\gamma}$. Insets match intensity profiles between two matrix diffraction spots and through the central beam. Note that the intensity of precipitate reflection peaks relative to that of the matrix peaks is higher in two-beam condition than in multi-beam condition. (e) CDF- and (f) CBF-TEM images taken respectively from the reflection positioned at $-1/3$ from the distance between (000) and $(02-2)_{\gamma}$ under $\mathbf{B} \sim [011]_{\gamma}$ and $\mathbf{g} = [200]_{\gamma}$ and with $\mathbf{B} \sim [011]_{\gamma}$ and $\mathbf{g} = [200]_{\gamma}$.

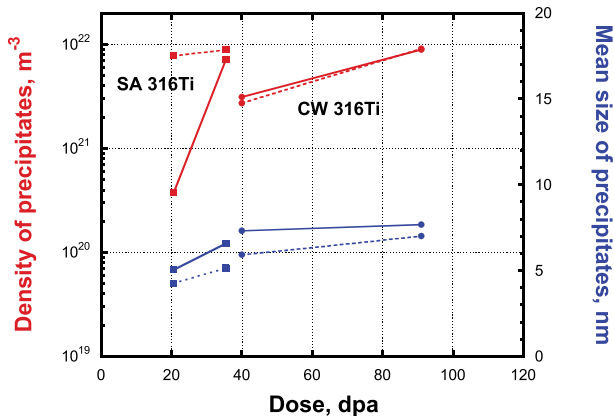


Fig. 15. Evolution of the density and mean size of precipitates observed in SA and CW 316Ti as a function of dose without stress during irradiation. These precipitates were visualized using high contrast Moiré fringe imaging (continuous lines) and CDF-TEM imaging (dashed lines).

4. Summary and discussion

4.1. Microstructural observations

The data presented in this paper show the effect of stress applied under irradiation on microstructure, thus providing a way of identifying the microstructural components involved during the linear regime of irradiation creep. Dislocation line segments, Frank loops, precipitates and twins were present in the microstructure of the different austenitic steels irradiated with and without stress. Considering that the detection limit of cavities (voids and/or bubbles) is around 1 nm, no cavity formation was found in stressed and unstressed specimens. This is in good agreement with the observations performed by Edwards et al. and Yang et al. [34,42]. This means that in the irradiation conditions of the study, irradiation creep occurs without swelling. The conclusions about twins, dislocation lines and loops, and precipitates can be drawn as follows.

The dislocation microstructure seems not to be significantly different between stressed and unstressed specimens. CW steels contain twins, which are unaffected by irradiation and stress.

Despite the varying chemistry and metallurgical state of

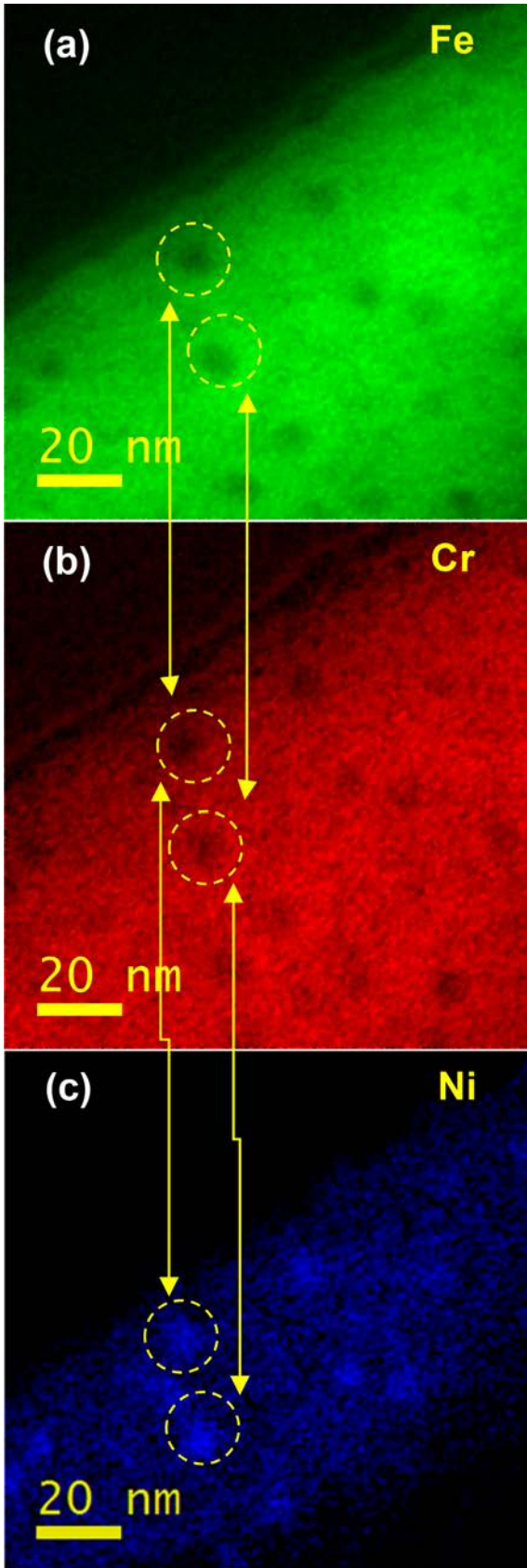


Fig. 16. EF-TEM images of CW316Ti irradiated to 91 dpa without stress. (a) Fe $L_{2,3}$, (b) Cr $L_{2,3}$ and (c) Ni $L_{2,3}$ elemental maps. Note that the areas of interest are taken in a low thickness (here, typically 10–50 nm) to reduce contribution of the γ matrix and thus to reveal the presence of precipitate thin platelets.

unstressed specimens, Frank loop characteristics (size and density) were found to be similar after irradiation, at least at 320 °C.

For most of the grades investigated, but CW 316Ti, the mean loop size is larger and the loop density lower in stressed materials than in unstressed materials. Except for CW HP316, no evidence of a clear and large anisotropy of Frank loop density or size induced by stress was found systematically. These results are in contradiction with some results of the open literature which show that the applied stress influences the partitioning of the loops on different {111} lattice planes, with or without effect on the overall loop density and/or average size [9,10,22]. As observed in CW HP316 irradiated with stress, Okamoto et al. [9] revealed differences in planar loop densities as large as a factor of two. Unfortunately, they have not carried out TEM observations on the Frank loop microstructure induced without stress for comparison. In the present work, the overall loop density with stress applied under irradiation can decrease by a factor of 2.3–5.7.

It should be noted that studies on the effect of stress on the microstructure of dislocations were often carried out at very low doses [22–27,31,32]. In this dose level and without stress, there is little or no interaction between Frank loops and perfect dislocations (rare dislocations and dislocation network with dislocation cells of 0.2–1 μm in diameter for weakly irradiated SA and CW materials, respectively). The high doses used in the present work strictly correspond to the steady-state density and mean size of Frank loops. At these doses, there are no differences of network dislocation microstructure between SA steels and CW steels. Dislocation lines (or rather segments) are distributed homogeneously. Independently of the initial microstructure and without stress, the fact that the loop density and size quickly reach a steady-state value and that the loops are surrounded by many dislocation segments suggests that the loop unfaults in contact with a glissile dislocation or with another Frank loop [1,10]. The empirical relationship of mean loop size s to total dislocation density ρ_T , $\langle s \rangle = \rho_T^{-1/2}$, takes into account this phenomenon. With stress, the absence of systematic anisotropy of loop densities or sizes at high doses implies that SIPN or SIPA process either declines with doses (underlying phenomenon) or does not appear in network-dominated microstructure.

Closely spaced precipitates, which occur in high number density, were sometimes observed. γ' -type precipitates formed in SA N9 whereas no precipitates or carbides/G-silicides formed in the other steel grades. For example, in CW 316Ti, it may be G-phase with a lattice parameter smaller than that of classical G-phase precipitates. Whatever the initial state of specimens, they are distributed homogeneously.

Precipitates tend to become larger and more numerous with a stress applied under irradiation. Besides, Katoh and coworkers [13] examined 4 MeV nickel ion irradiated ribbon tensile specimens of SA 316 stainless steel. Irradiation occurred up to 50 dpa at 600 °C for stresses between 0 and 200 MPa. Apart Frank loops, network dislocations and cavities, needle-like precipitate particles were observed. These precipitates are neither quantitatively analyzed nor identified, but showed a tendency to get large and coarse with increasing stress. This growth of precipitates enhanced by creep was also reported by Morris and Harries [64]. They examined thermal creep response in initially SA Type 316 austenitic stainless steel specimens tested at temperatures in the range 525–900 °C. It was found that the rates of precipitation of τ -carbides and intermetallic phases were increased by factors of about 10 and 3, respectively, with intragranular precipitation being much more extensive in the strained steel than in the unstrained steel. The enhancement of the precipitation kinetics has been interpreted as a consequence of the moving dislocations which provide more extensive intragranular nucleation sites and faster diffusion paths (effect of solute drag).

Table 6

Precipitate density and mean size in various unstressed austenitic steel grades after irradiation between 18 and 35 dpa.

	Metallurgical steel	Dose, dpa	Type of precipitates	Density, $\times 10^{21} \text{ m}^{-3}$	Mean size, nm
304L	SA	20	τ , η and/or G*	0.3	6.9
316Ti		35		7.2	6.6
N9		17.7	γ' **	Not measured	
NMF18	CW	19.5	Absent or rare		
321		17.5			
316		20	τ , η and/or G*	6.1	5.7
316Ti		40		3.1	7.3
HP316		20	Absent or rare		
HP316Si					

Notes: * indicates that the precipitates formed during irradiation were visualized using Moiré fringe imaging and **using CDF-TEM imaging. There are isolated and coarse TiC carbides in SA 321 before and after irradiation. At least for CW 316Ti, it may be G-phase precipitates with a lattice parameter smaller than that of classical G-phase precipitates. The specimens such as SA 304L and 316 @ 20 dpa, SA 316Ti @ 35 dpa and CW 316 @ 40 dpa were studied in previous research works [37,38].

For some steel grades such as CW 316 and SA 304L, the discrepancy between precipitate and Frank loop densities is less important under stressed conditions than under unstressed conditions, whereas for CW 316Ti, it remains almost constant.

4.2. Irradiation creep behavior

For a given stress level, the diametrical strain increases linearly with increasing doses. This strain depends on the stress level. The higher the stress level is, the higher the steady-state irradiation creep rate is. Even in the absence of swelling, creep behavior depends sensibly to the chemical composition and metallurgical state of steels. According to the initial state of steel, the steady-state irradiation creep compliance can vary from 2 to $4.2 \times 10^{-6} \text{ MPa}^{-1} \text{ dpa}^{-1}$.

The data from these irradiation creep tests with fast neutrons and up to 8% of effective strain are unique. Indeed, they make it clear that irradiation creep rate without swelling can decrease with increasing cold-working level (CW 316Ti versus SA 316Ti). Alloy composition can also affect this rate. The creep behavior differences related to these two parameters are especially visible at high dose levels and for stresses ranging from 127 to 220 MPa. Toloczko et al. [65] indicated that the irradiated creep compliance B_0 may be mildly sensitive to alloy composition. Grossbeck et al. [66] also investigated the effect of cold work for type 316 stainless steels and PCA alloys. On the basis of effective strain results obtained at lower values (up to ~1.6%), the creep compliance values B_0 for 316 SS in the SA and 20% CW conditions and for PCA alloys in the SA and 25% CW conditions were found to be almost similar. Therefore, the investigators cited above concluded that cold work did not affect the value of B_0 .

For each grade and at a given stress, the sample exhibits a threshold dose of a few dpa. By comparing with creep data in the literature, this incubation may correspond to shrinkage. And this shrinkage is usually said to be due to carbide-induced densification [6,16,67–69]. The microstructure of neutron-irradiated austenitic steels contains high densities of faulted dislocation loops, precipitates (γ' in SA N9, G-phase in CW 316Ti and not rigorously identified precipitates (probably τ , η and/or G) in other steel grades) and dislocation segments. Here, at a temperature of at least 320 °C, precipitates do not appear systematically in all our steel grades. Shrinkage could not be only attributed to the formation of carbides. However, one must take into consideration other types of precipitates, restoration or formation of the dislocation network or intragranular segregation phenomenon on various defect sinks [45,70–72], which could induce negative lattice parameter variations.

4.3. Possible microscopic mechanisms of irradiation creep

Several irradiation creep models directed at understanding the behavior of different types of materials have been identified so far [46]. At the present, three of them have wide supports for austenitic steels: SIPN, SIPA and SICG [8,11,20,21,23–26,46–49]. In the SIPN mechanism of irradiation creep, the application of an external stress can enhance the probability of interstitial loops nucleating on planes with a preferred orientation. The SIPA creep mechanism enables the transfer of atoms from planes parallel to the applied stress to those perpendicular to the applied stress. Therefore, SIPA corresponds to the net preferred absorption of interstitials at dislocation loops and lines. While SIPA provides a mechanism for creep by dislocation climb, dislocations can also contribute to creep by glide. This glide can be driven by climb process (SICG).

The SIPA mechanism normally predicts a linear stress dependence of creep strain. However, microstructural results of this work have shown that not only SIPA but also SIPN process either decline with doses (underlying phenomenon) or do not appear in network-dominated microstructure. Indeed, no evidence of a clear and large anisotropy of Frank loop density or size induced by stress was found systematically. Often, with stress applied during irradiation, the mean loop size is larger and the loop density per plane $\{111\}_\gamma$ lower.

Initially, a mechanism based on climb-controlled glide was forwarded by Harkness et al. [73]. This mechanism was developed to account for the climb of dislocations over dispersed obstacles by the absorption of irradiation-induced point defects. However, just after the proposal of this mechanism, the attention of experimenters was quickly diverted to anisotropy in Frank loop populations where effects of stress on loop populations could be sometimes observed. Depending on the parameters chosen, various climb-enhanced glide mechanisms describing the irradiation creep rate have been published [47].

Its dependence in stress can be parabolic, linear or quadratic. It is quadratic if the variation in rate arises from the climb distance to initiate glide and not from any stress dependence of climb velocity and only when the volume fraction rate of cavities is constant. Wolfer et al. [74] have developed a model in which dislocation loops serve as dominant glide obstacles. For them, irradiation creep by climb controlled glide is expected to be proportional to $\sigma^{1/2}$ at low stresses but to become linearly dependent on the stress for higher stresses. Nevertheless, the researchers have considered that this microscopic mechanism occurs mainly during the transient period of irradiation creep. The concept of climb-enabled glide is also recognized when one considers that excess interstitials may flow into dislocations in the absence of cavities, if an excess of vacancies is absorbed by other sinks.

As indicated in the part 4.1., Morris and Harries [64] observed an effect of stress on the precipitation rates. This enhancement of the

kinetics was associated to the moving of dislocations (solute drag effects). From this study and the current work, the following mechanism appears thus to be operating. In the absence of stress and whatever the starting microstructure, there are a dynamic equilibrium between the production of dislocations and their recovery beyond 3–5 dpa. A larger rate of gliding dislocations and thus a higher precipitation kinetic might be induced by an external stress applied under irradiation. This is compatible with an increase of the density and average size of precipitates in strained steels compared to unstrained steels.

Gilbert et al. [75] have theoretically proposed the unfauling of Frank loops and their subsequent gliding as a creep mechanism under irradiation. As to Yang et al. [76], they carried out molecular dynamics simulations of compression processes out for copper lattices containing one Frank loop. Their results showed that both interstitial and vacancy type Frank loops became sources of dislocation under stress, and accompanying unfauling process, Frank loops were broken up instead of becoming perfect loop.

If dislocation glide corresponds to the microscopic mechanism of irradiation creep in the current study, mobile dislocations should interact with Frank loops. In other words, the presence of moving network dislocations should unfaul Frank loops and preclude the long-term survival of larger Frank loops. This is consistent with the lower Frank loop density but not with the larger loops observed in our stressed specimens compared to our unstressed specimens.

Nevertheless, because the mean loop size approaches a value equal to $\rho_T^{-1/2}$, where ρ_T is the total dislocation line density [1], one could conclude that Frank loops continue to grow with a lower loop density with a similar perfect dislocation density.

According to Jitsukawa et al. [12], the remaining Frank loop density after electron irradiation at 450 °C with stress is lower. They observed that (i) Frank loops nucleated without external load react with Shockley partial dislocations induced by external load to be perfect loops, (ii) the growth of the unfauled loops by radiation-induced climb occurs up to a critical size and (iii) the growth rate of perfect loops is indeed enhanced by increases in the normal stress on the loop plane. These observations led the researchers to the conclusion that the glide of these unfauled loops play an important role for creep deformation under irradiation. Growth of perfect loops has been thought to be due to climb absorbing interstitial atoms.

It was also shown that according to the value of stacking fault energy (SFE), moving dislocations could be dissociated into Shockley partial dislocations during glide. These partial dislocations are separated by stacking faults. The lower SFE value tends to promote the nucleation of the separated Shockley partials from glide dislocations or of a Shockley partial inside the Frank loop. Increased SFE enhances cross-slip [77] and thus the likelihood of loop unfauling. Therefore, alloy constituents that increase the SFE should increase the non-swelling creep compliance B_0 .

In order to confirm or disprove this assumption, Gilbert et al. [78,79] recapitulated the value of in-reactor creep rate and SFE of all the stainless steels published in the open literature. They reported that SFE depending on the composition of steel can be an important parameter affecting the non-swelling creep modulus. The irradiation creep compliance was found to increase with increasing SFE. Most of the investigated pressurized tubes were irradiated between 330 and 420 °C.

Table 7 shows the values of irradiation creep compliance and SFE of our investigated steels for a wide range of stress and dose levels. One can note that Pickering formula does not provide the same results as that of Gilbert. With Pickering formula [80], no direct correlation between the value of SFE and the steady-state creep rate was found. Gilbert formula [78] provides very similar SFE values for SA 304L, CW 316 and CW 316Ti whereas these steel

grades have relatively different steady-state creep compliance values. CW N9 which has the higher SFE value creeps faster than other steels. According to Gilbert et al. [78], the higher the value of SFE is, the higher the in-reactor creep compliance is.

This correlation must be considered carefully. At least at 320–330 °C and for CW 316, the creep rate given by them (at 7.4 dpa and up to 300 MPa, $B_0 = 1.3 \times 10^{-6} \text{ MPa}^{-1} \text{ dpa}^{-1}$, $\text{SFE} = 22.8 \text{ mJ/m}^2$) is slightly lower than that given in this work (between 20 and 86 dpa and up to 188 MPa, $B_0 = 2.55 \times 10^{-6} \text{ MPa}^{-1} \text{ dpa}^{-1}$, $\text{SFE} = 13.2 \text{ mJ/m}^2$), by Foster et al. [16] (between ~0.02 and 0.54 dpa and at 345 MPa, $B_0 = 2.6 \times 10^{-6} \text{ MPa}^{-1} \text{ dpa}^{-1}$) and by Garner [81] (at 13.1 dpa and up to ~400 MPa, $B_0 = 2.8 \times 10^{-6} \text{ MPa}^{-1} \text{ dpa}^{-1}$). Pickering and Gilbert formulas cannot be used for example for NMF 18. Indeed, the calculated SFE is negative.

It should be noted that the calculated value of SFE does not take into account the starting metallurgical state whereas this work has revealed that the creep behavior depends on this state. Moreover, through precipitation induced by irradiation, the value of SFE of the γ matrix may change.

According to hypothesis that larger Frank loops have larger SFE, they should be unfauled more easily. This is not in agreement with our experimental results and those given by Ando et al. [82]. TEM observations performed by these researchers on irradiated stainless steel showed that, after indentation, Frank loops smaller than 20 nm in diameter completely disappeared in heavily plastically deformed regions whereas larger ones survived. It should be noted that indentation was carried out after irradiation and thus interstitials and vacancies were no longer produced during this test, which could lead to slightly different results compared to those obtained from irradiation creep tests.

If we consider that deformation occurs by the dislocation glide after climb over dispersed obstacles such as precipitates, dislocation reactions with different precipitate densities should rationalize irradiation creep rates (climb-controlled glide). In fact, the linear character of important creep deformation observed in the current study would imply that the precipitate microstructure should reach a steady state.

Unlike Frank loops, the density and size of precipitates were not found to be strictly similar at each dose level for a given unstressed stainless steel. Moreover, in very highly irradiated specimens of SA 304L and CW 316Ti (≥ 91 dpa), SAD patterns have shown additional precipitate reflection spots.

Or else, the precipitation has no direct causative effect on creep. In other words, the precipitate effect can be of second-order importance compared to other microstructural barriers. Precipitation may be concurrent with creep since precipitates appear larger and more numerous in stressed steels.

A different steady-state creep rate was observed between SA and CW 316Ti for which the precipitate microstructure was not very different. As the perfect dislocation microstructure has been thought not to be different between SA and CW steels after irradiation, a higher fraction of twins (that lead to the reduction of the mean path of dislocations (Hall-Petch effect)) could reduce the creep rate [83,84]. In principle, gliding dislocations could occur with more difficulty in the presence of many Frank loops acting as barriers to these perfect dislocations. Nevertheless, these nanosized barriers could be bypassed by means of climbing dislocations. Climb-controlled glide process of dislocation could thus be partially affected by the presence of twins. Twins are barriers bigger than Frank loops.

5. Conclusions

The goal of investigating this wide variety of materials is to

evaluate the effect of both metallurgical state and chemical elements on irradiation creep behavior and radiation-induced microstructure/microchemistry. This work has enabled us to provide more information on the possible mechanisms of strain induced by stress applied under irradiation at the micro/nanometer scale. These materials correspond to different austenitic steel grades. They were irradiated at 320 °C up to 120 dpa with and without a stress ranging from 0 to 220 MPa in the BOR-60 fast reactor. Each stress corresponds to a specific pressurized tube specimen.

(2) Microstructure and microchemistry can exhibit considerable differences.

Without stress applied during irradiation, no notable differences were found for Frank loops in terms of number density and mean size between different steel grades. Nanoscale precipitates were observed. Their density and size depend on the initial state of different steels, i.e., metallurgical state and alloying composition. Frank loops and precipitates are surrounded by a high density of dislocation segments. Whatever the initial metallurgical state,

Table 7
Values of irradiation creep compliance and stacking fault energy of investigated steels.

Steel grades	$B_0, 10^{-6} (\text{MPa dpa})^{-1}$	Pickering Formula [81]	Gilbert formula [79]
CW N9	4.15	82.1	54.6
SA 304L	3.55	26.2	14.5
CW 316	2.55	42.1	13.2
CW 316Ti	1.97	44.2	13

The following conclusions can be drawn from the Results and Discussion:

(1) Irradiation creep of austenitic steels is linear in dose and stress. It is relatively sensitive to their metallurgical state and chemical composition. According to the initial state of steel, the irradiation creep compliance can vary from 2 to $4.2 \times 10^{-6} \text{MPa}^{-1} \text{dpa}^{-1}$.

Frank loops, precipitates and dislocation segments are distributed homogeneously.

Often, with stress applied during irradiation, the mean loop size is larger and the loop density lower. No evidence of a clear and large anisotropy of Frank loop density or size induced by stress was found systematically. Precipitates appear to become larger and more numerous in stressed materials.

In addition to the different microstructural components induced by irradiation, CW steels contain twins, which are unaffected by

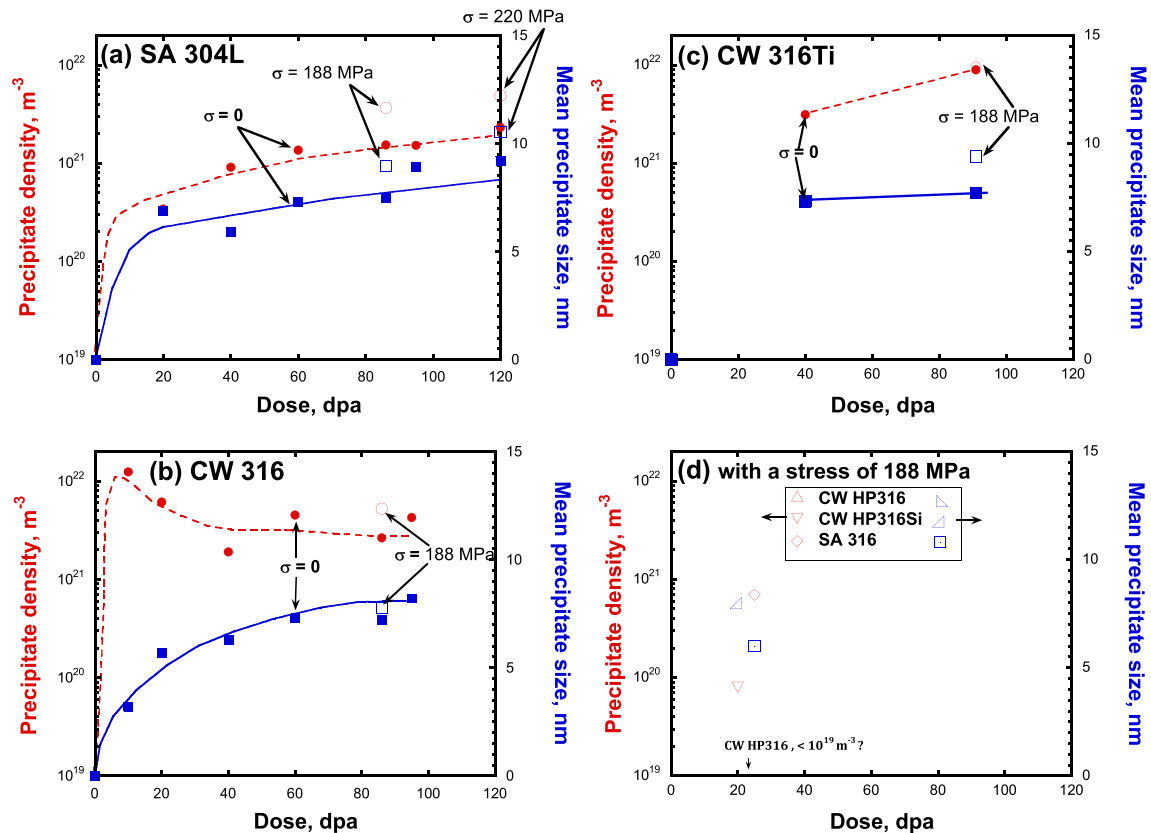


Fig. 17. Evolution of the precipitate density (dashed lines) and mean size (continuous lines) in (a) SA 304L, (b) CW 316, (c) CW 316Ti, (d) CW HP316, CW HP316Si and SA 316 as a function of dose with (open dots) or without (filled dots) a stress ranging from 188 to 220 MPa [37,38].

irradiation and stress.

- (3) The systematic study of the effect of stress applied under irradiation on the mechanical behavior and the corresponding microstructure has enabled us to establish that irradiation creep depends on at least two parameters:

-Twins from cold working that appear to limit the irradiation creep rate. Hardening should not be analyzed in terms of dislocations in large doses. Indeed, following the multiplication and recovery of dislocation lines and loops, the microstructure of dislocations is not different between SA and CW materials; -The nickel content. A lower nickel content (~9.5–13% instead of 25%wt) attenuates the creep rate; A relatively large irradiation creep results in a decrease in the density of Frank loops and an increase in their size and an increase in the density and size of precipitates.

Acknowledgements

The authors wish to thank gratefully Dr. V. Golovanov and Prof. V. Shamardin at RIAR, Russia, for conducting neutron irradiation in BOR-60 reactor and post-irradiation creep testing. They wish also to thank J.P. Massoud (EdF) and Ph. Dubuisson (CEA) who are at the origin of the experiments reported in this study. Special thanks are given to B. Verhaeghe for their efforts of preparation of the TEM disks characterized in this study, Th. Van den Berghe for receiving and stocking these disks and B. Arnal for particle counting.

Appendix

In a first approximation, the tangential strain could be estimated with respect to the relative evolution of the external diameter D^{ext} as follows:

$$\varepsilon_{\theta}^{(1)} = \frac{D^{ext} - D_0^{ext}}{D_0^{ext}}$$

where D_0^{ext} is the initial external diameter of the tube. This expression provides a good approximation for thin-walled tubes and is easy to compute since it only uses measurable dimensions. For thicker-walled tubes, it is better to use the average diameter:

$$D^{av} = \frac{D^{ext} + D^{in}}{2}$$

where D^{in} is the internal diameter of the tube. The tangential strain can subsequently be calculated using:

$$\varepsilon_{\theta}^{(2)} = \frac{D^{av} - D_0^{av}}{D_0^{av}}$$

Since $D^{in} = D^{ext} - t$, where t is the wall thickness:

$$\varepsilon_{\theta}^{(2)} = \frac{(D^{ext} - t) - (D_0^{ext} - t_0)}{D_0^{ext} - t_0} = \frac{(D^{ext} - D_0^{ext})}{D_0^{ext} - t_0} - \frac{(t - t_0)}{D_0^{ext} - t_0}$$

For a thin-walled tube, due to the volume conservation, $\varepsilon_{\theta} = -\varepsilon_r$ where $\varepsilon_r = \frac{t-t_0}{t_0}$:

$$\varepsilon_{\theta}^{(2)} = \frac{(D^{ext} - D_0^{ext})}{D_0^{ext} - t_0} + \varepsilon_{\theta}^{(1)} \frac{t_0}{D_0^{ext} - t_0}$$

$$\varepsilon_{\theta}^{(2)} \left(1 - \frac{t_0}{D_0^{ext} - t_0} \right) = \frac{(D^{ext} - D_0^{ext})}{D_0^{ext} - t_0}$$

$$\varepsilon_{\theta}^{(2)} = \frac{(D^{ext} - D_0^{ext})}{D_0^{ext} - 2t_0} = \varepsilon_{\theta}^{(1)} \frac{D_0^{ext}}{D_0^{ext} - 2t_0}$$

References

- [1] H.R. Brager, F.A. Garner, E.R. Gilbert, J.E. Flinn, W.G. Wolfer, Radiation Effects in Breeder Reactor Structural Materials, The Metallurgical Society of AIME, 1977, pp. 727–755.
- [2] F.A. Garner, D.L. Porter, B.J. Makenas, J. Nucl. Mater. 148 (1987) 279.
- [3] D.L. Porter, G.D. Hudman, F.A. Garner, J. Nucl. Mater. 179 (1991) 581.
- [4] V.S. Neustroev, V.K. Shamardin, Effects of Radiation on Materials, in: 19th International Symposium, ASTM STP 1366, 2000, pp. 645–654.
- [5] S.I. Porollo, A.N. Vorobjev, YuV. Konobeev, N.I. Budylnin, E.G. Mironova, F.A. Garner, Effects of Radiation on Materials, in: 19th International Symposium, ASTM STP 1366, 2000, pp. 679–687.
- [6] J.P. Foster, K. Bunde, D.L. Porter, J. Nucl. Mater. 317 (2003) 167.
- [7] E.R. Gilbert, F.A. Garner, J. Nucl. Mater. 367–370 (2007) 954.
- [8] S. Ukai, S. Ohtsuka, J. Nucl. Sci. Technol. 44 (5) (2007) 743.
- [9] P.R. Okamoto, S.D. Harkness, J. Nucl. Mater. 48 (1973) 204.
- [10] H.R. Brager, F.A. Garner, G.L. Guthrie, J. Nucl. Mater. 66 (1977) 301.
- [11] D.S. Gelles, F.A. Garner, H.R. Brager, Effects of Radiation on Materials, in: 10th International Symposium, ASTM STP 725, 1981, pp. 735–753.
- [12] S. Jitsukawa, Y. Katano, K. Shiraiishi, J. Nucl. Sci. Technol. 21 (9) (1984) 671.
- [13] Y. Katoh, Y. Kohno, A. Koyama, Effects of Radiation on Materials, in: 16th International Symposium, ASTM STP 1175, 1993, pp. 978–991.
- [14] V.S. Neustroev, E.I. Makarov, S.V. Belozero, Z.E. Ostrovky, Proceedings of Fontevraud VII Symposium on Contribution of Materials Investigations to Improve the Safety and Performance of LWRs, SFEN, 2010, N°006-A065-T02.
- [15] M.L. Grossbeck, J.A. Horak, J. Nucl. Mater. 155–157 (1988) 1001.
- [16] J.P. Foster, T. Karlsen, in: Proceedings of the 14th International Conference on Environmental Degradation of Materials in Nuclear Power Systems-Water Reactors, ANS, 2009, pp. 1355–1370.
- [17] J.P. Foster, T.M. Karlsen, in: Proceedings of the 15th International Conference on Environmental Degradation of Materials in Nuclear Power Systems-Water Reactors, TMS, 2011, pp. 1339–1350.
- [18] J. Garnier, P. Dubuisson, C. Pokor, E. Lemaire, N. Monteil, J.P. Massoud, in: Proceedings of Fontevraud VII Symposium on Contribution of Materials Investigations to Improve the Safety and Performance of LWRs, SFEN, 2010, N°014-A150-T02.
- [19] J. Garnier, Y. Bréchet, M. Delnondedieu, C. Pokor, P. Dubuisson, A. Renault, J.P. Massoud, J. Nucl. Mater. 413 (2011) 63.
- [20] D.J. Michel, P.L. Hendrick, A.G. Pieper, Irradiation Effects on the Microstructure and Properties of Metals, ASTM STP 611, 1976, pp. 284–297.
- [21] D.J. Michel, P.L. Hendrick, A.G. Pieper, J. Nucl. Mater. 75 (1978) 1.
- [22] D. Caillard, J.L. Martin, B. Jouffrey, Ann. Chim. Fr. 6 (1981) 37–45.
- [23] T. Atkins, R.J. McElroy, Effects of Radiation on Materials, in: Eleventh Conference, ASTM STP 782, 1982, pp. 841–855.
- [24] C.H. Henager Jr., E.P. Simonen, E.R. Bradley, R.G. Stang, J. Nucl. Mater. 117 (1983) 250.
- [25] C.H. Henager Jr., E.P. Simonen, E.R. Bradley, R.G. Stang, J. Nucl. Mater. 122–123 (1984) 413.
- [26] T. Atkins, R.J. Mc Elroy, Radiation-induced Changes in Microstructure, in: 13th International Symposium (Part 1), ASTM STP 955, 1987, pp. 447–465.
- [27] H. Saka, K. Kawamura, Y. Morozumi, H. Teshima, J. Nucl. Mater. 179–181 (1991) 966.
- [28] K. Ueno, J. Nagakawa, Y. Murase, N. Yamamoto, J. Nucl. Mater. 329–333 (2004) 602.
- [29] C. Pokor, Y. Bréchet, P. Dubuisson, J.P. Massoud, A. Barbu, J. Nucl. Mater. 326 (2004) 19.
- [30] C. Pokor, Y. Thebault, J.P. Massoud, M. Delnondedieu, D. Loinsard, P. Dubuisson, J. Kocik, E. Keilova, E. Lemaire, in: Proceedings of Fontevraud VI Symposium on Contribution of Materials Investigations to Improve the Safety and Performance of LWRs, SFEN, 2006, p. 615.
- [31] F.A. Garner, D.S. Gelles, J. Nucl. Mater. 159 (1988) 286.
- [32] D.S. Gelles, J. Nucl. Mater. 205 (1993) 146.
- [33] D.J. Edwards, E.P. Simonen, F.A. Garner, L.R. Greenwood, B.M. Oliver, S.M. Bruemmer, J. Nucl. Mater. 317 (2003) 32.
- [34] D. Edwards, E. Simonen, S. Bruemmer, P. Efsing, in: Proceedings of Fontevraud VI Symposium on Contribution of Materials Investigations to Improve the Safety and Performance of LWRs, SFEN, 2006, p. 603.
- [35] K. Fukuya, K. Fujii, H. Nishioka, Y. Kitsunai, J. Nucl. Sci. Technol. 43 (2006) 159.
- [36] Y. Isobe, M. Sagisaka, F.A. Garner, S. Fujita, T. Okita, J. Nucl. Mater. 386 (2009) 661.
- [37] A.E. Renault, C. Pokor, J. Garnier, J. Malaplate, in: Proceedings of the 14th International Conference on Environmental Degradation of Materials in

- Nuclear Power Systems-Water Reactors, ANS, 2009, pp. 1324–1334.
- [38] A. Renault, J. Malaplate, C. Pokor, P. Gavaille, J.P. Massoud, J. Garnier, in: Proceedings of Fontevraud VII Symposium on Contribution of Materials Investigations to Improve the Safety and Performance of LWRs, SFEN, 2010, N°O10-A023-T02.
- [39] A. Renault, J. Malaplate, C. Pokor, P. Gavaille, J. Nucl. Mater. 421 (2012) 124–131.
- [40] A. Renault-Laborne, J. Malaplate, C. Pokor, B. Tanguy, Effects of Radiation on Materials, in: 26th International Symposium, ASTM STP 1572, 2014, pp. 74–97.
- [41] A. Renault-Laborne, P. Gavaille, J. Malaplate, C. Pokor, B. Tanguy, J. Nucl. Mater. 460 (2015) 72.
- [42] Y. Yang, Y. Chen, Y. Huang, T. Allen, A. Rao, in: Proceedings of 15th International Conference on Environmental Degradation of Materials in Nuclear Power Systems-Water Reactors, TMS, 2011, pp. 2137–2148.
- [43] A. Etienne, B. Radiguet, P. Pareige, J. Nucl. Mater. 406 (2) (2010) 251.
- [44] T. Toyama, Y. Nozawa, W. Van Renterghem, Y. Matsukawa, M. Hatakeyama, Y. Naga, A. Al Mazouzi, S. Van Dyck, J. Nucl. Mater. 418 (2011) 62.
- [45] Y. Chen, P.H. Chou, E.A. Marquis, J. Nucl. Mater. 451 (2014) 130.
- [46] J.R. Matthews, M.W. Finnis, J. Nucl. Mater. 153 (1988) 257.
- [47] L.K. Mansur, T.C. Reiley, J. Nucl. Mater. 90 (1980) 60.
- [48] M.B. Toloczko, J.P. Hirth, F.A. Garner, J. Nucl. Mater. 283–287 (2000) 409.
- [49] J. Garnier, Y. Bréchet, M. Delnondedieu, A. Renault, C. Pokor, P. Dubuisson, J.P. Massoud, J. Nucl. Mater. 413 (2011) 70.
- [50] C. Pokor, Y. Bréchet, P. Dubuisson, J.P. Massoud, A. Barbu, J. Nucl. Mater. 326 (2004) 30.
- [51] D.J. Edwards, E.P. Simonen, S.M. Bruemmer, J. Nucl. Mater. 317 (2003) 13.
- [52] Y. Yang, Y. Chen, T. Allen, O.K. Kopra, in: Proceedings of the 14th International Conference on Environmental Degradation of Materials in Nuclear Power Systems-Water Reactors, ANS, 2009, pp. 1335–1340.
- [53] C. Cawthorne, C. Brown, J. Nucl. Mater. 66 (1977) 201.
- [54] W.J.S. Yang, Radiation-induced Changes in Microstructure, in: 13th International Symposium, ASTM STP 955, 1987, pp. 628–646.
- [55] T. Kimoto, T. Saito, J. Nucl. Mater. 212–215 (1994) 275.
- [56] B.H. Sencer, G.M. Bond, F.A. Garner, M.L. Hamilton, S.A. Maloy, W.F. Sommer, J. Nucl. Mater. 296 (2001) 145.
- [57] T.M. Williams, J.M. Titchmarsh, D.R. Arkell, J. Nucl. Mater. 82 (1979) 199.
- [58] W.J.S. Yang, H.R. Brager, F.A. Garner, in: Proceedings, Symposium on Phase Stability During Irradiation, The Metallurgical Society of AIME, 1981, pp. 257–269.
- [59] L.E. Thomas, J.M. Beeston, J. Nucl. Mater. 107 (1982) 159.
- [60] T.M. Williams, J.M. Titchmarsh, D.R. Arkel, J. Nucl. Mater. 107 (1982) 222.
- [61] A. Mateo, L. Llanes, M. Anglada, A. Redjaimia, G. Metauer, J. Mater. Sci. 32 (1997) 4533.
- [62] I. Shuro, H.H. Kuo, T. Sasaki, K. Hono, Y. Todaka, M. Umemoto, Mater. Sci. Eng. 552 (2012) 194.
- [63] S. Li, Y. Wang, X. Wang, F. Xue, J. Nucl. Mater. 452 (2014) 382.
- [64] D.G. Morris, D.R. Harries, Met. Sci. 12 (1978) 542.
- [65] M.B. Toloczko, F.A. Garner, J. Standring, B. Monro, S. Adaway, J. Nucl. Mater. 258–263 (1998) 1606.
- [66] M.L. Grossbeck, L.T. Gilbson, S. Jitsukawa, L.K. Mansur, L. Turner, Effects of Radiation on Materials, in: 18th International Symposium, ASTM STP 1325, 1999, pp. 725–741.
- [67] J.L. Straalsund, M.M. Paxton, Nucl. Technol. 13 (1972) 99.
- [68] J.F. Bates, M.M. Paxton, J.L. Straalsund, Nucl. Technol. 20 (1973) 134.
- [69] J.A. Spitznagel, R. Stickler, Metal. Trans. 5 (1974) 1363.
- [70] A. Etienne, B. Radiguet, N.J. Cunningham, G.R. Odette, P. Pareige, J. Nucl. Mater. 406 (2010) 244.
- [71] Z. Jiao, G.S. Was, Acta. Mater. 59 (2011) 1220.
- [72] Z. Jiao, G.S. Was, J. Nucl. Mater. 449 (2014) 200.
- [73] S.D. Harkness, J.A. Tesk, C.-Y. Li, Nucl. Appl. Technol. 1 (1970) 24.
- [74] W.G. Wolfer, A. Boltax, in: Proceedings of the BNES Conference on Irradiation Embrittlement and Creep in Fuel Cladding and Core Components, The Metallurgical Society of AIME, 1972, p. 283.
- [75] E.R. Gilbert, J.J. Holmes, Trans. Am. Nucl. Soc. 13 (1970) 609.
- [76] Y. Yang, H. Abe, N. Sekimura, Phys. Lett. A 315 (2003) 293.
- [77] B. Escaig, Dislocation Dynamics, Mc Graw Hill, New York, 1968, p. 655.
- [78] E.R. Gilbert, J.P. Foster, J. Nucl. Mater. 298 (2001) 321.
- [79] E.R. Gilbert, J.P. Foster, J. Nucl. Mater. 300 (2002) 90.
- [80] F.B. Pickering, in: Proceedings of the Conference on Stainless Steels, vol. 84, The Institute of Metals, 1985, p. 2.
- [81] F.A. Garner, Radiation damage in austenitic steels, in: R.J.M. Konings (Ed.), Comprehensive Nuclear Materials, vol. 4, Elsevier, 2012, pp. 33–95.
- [82] M. Ando, Y. Katoh, H. Tanigawa, A. Kohyama, T. Iwai, J. Nucl. Mater. 283–287 (2000) 423.
- [83] S. Allain, Ph. D. Thesis, Institut National Polytechnique de Lorraine, 2004.
- [84] D. Maréchal, Ph. D. Thesis, Institut National Polytechnique de Grenoble, 2004.